ELSEVIER

Dynamics of Atmospheres and Oceans 29 (1999) 255–303

dynamics of atmospheres and oceans

www.elsevier.com/locate/dynatmoce

Estimation and study of mesoscale variability in the strait of Sicily

P.F.J. Lermusiaux *

Harvard University, 29 Oxford Street Cambridge, MA 02138 USA

Received 17 July 1998; received in revised form 13 January 1999; accepted 26 February 1999

Abstract

Considering mesoscale variability in the Strait of Sicily during September 1996, the four-dimensional physical fields and their dominant variability and error covariances are estimated and studied. The methodology applied in real-time combines an intensive data survey and primitive equation dynamics based on the error subspace statistical estimation approach. A sequence of filtering and prediction problems are solved for a period of 10 days, with adaptive learning of the dominant errors. Intercomparisons with optimal interpolation fields, clear sea surface temperature images and available in situ data are utilized for qualitative and quantitative evaluations. The present estimation system is shown to be a comprehensive nonlinear and adaptive assimilation scheme, capable of providing real-time forecasts of ocean fields and associated dominant variability and error covariances. The initialization and evolution of the error subspace is explained. The dominant error eigenvectors, variance and covariance fields are illustrated and their multivariate, multiscale properties described. Five coupled features associated with the dominant variability in the Strait during August–September 1996 emerge from the dominant decomposition of the initial PE variability covariance matrix: the Adventure Bank Vortex, Maltese Channel Crest, Ionian Shelf Break Vortex, Strait of Messina Vortex, and subbasin-scale temperature and salinity fronts of the Ionian slope. From the evolution of the estimated fields and dominant predictability error covariance decompositions, several of the primitive equation processes associated with the variations of these features are revealed, decomposed and studied. In general, the estimation of the evolving dominant decompositions of the multivariate predictability error and variability covariances appears promising for ocean sciences and technology. The practical feedbacks of the present approach which include the determination of data optimals and the refinements of dynamical and measurement models are considered.

Keywords: Mesoscale variability; Strait of Sicily; Error covariances

* Tel.: +1-617-495-0378; e-mail: pierrel@pacific.harvard.edu

0377-0265/99/$ - see front matter
PII: S0377-0265(99)00008-1

1. Introduction

An essential activity in oceanography consists of estimating and studying the evolution, in space and time, of the physical, biological and geochemical properties of the sea (e.g., Defant, 1961). As in classical mechanics, one is then interested in the ocean fields, i.e., the functions of space and time characterizing the considered ocean state. In this paper, some simple steps are taken towards the extension of this fundamental view to the estimation and study of the evolution, in space and time, of the statistical properties of real ocean fields. For multivariate, multiscale and nonhomogeneous issues, the task is challenging. As a first endeavor, the investigation is restricted to the four-dimensional physical fields, a classic interest, and to the four-dimensional covariances of these fields. The methodology employed for this investigation combines real data and dynamics based on the Error Subspace Statistical Estimation (ESSE) approach (Lermusiaux, 1997). It was exercised in real-time during the operation Rapid Response 96 (RR96), considering mesoscale variability in the Strait of Sicily during August and September 1996. The real-time statistical estimation consisted of a series of prediction and filtering problems (Jazwinski, 1970) and the word estimation in this paper is used in this sense.

The North Atlantic Treaty Organization (NATO) operation RR96 was designed to demonstrate a rapid environmental assessment (REA) in a naval context (Pouliquen, 1997; Sellschopp and Robinson, 1997). Ocean surveys were carried out with several ships continuously sampling the region and aircrafts rapidly deploying temperature vs. depth probes (AXBTs). The main Harvard participation in RR96 consisted of the real-time nowcasting and forecasting of the physical fields, using the Harvard Ocean Prediction System (HOPS, e.g., Robinson, 1996). Several two-way nested sub-domains were employed for higher resolution estimation in coastal areas of specific interest. The products included primitive equation forecasts and data assimilation using Optimal Interpolation (OI), with real-time atmospheric forcing and acoustic computations. An overview of the experiment and a discussion of the Atlantic Ionian Stream (AIS) variability in the Strait is given in (Robinson et al., 1998b).

The intensive data of RR96 and the calibrated primitive equation model of HOPS provided an ideal test situation for ESSE. The physical fields, their variabilities, uncertainties and corresponding dominant covariances, were in fact predicted in real-time. Comparisons with the OI scheme were carried out, and, for the first time, several operational and scientific ESSE products were made available to NATO (W.G. Leslie, personal communication). Fig. 1 is one of these products, especially important for its use in real-time adaptive sampling. Panel (a) is the surface temperature on Sept. 18 after ESSE assimilation of hydrographic data sampled on that day. Panel (b) is the expected mesoscale error field of the assimilated data. Panel (c) is the error standard deviation of the map of Panel (a): it is obtained from the diagonal of the a posteriori error covariance matrix. After the assimilation, the largest surface temperature uncertainties (Panel c) are found in two regions: one (35–37°N, 12–14°E) is mainly associated with the so-called Maltese Channel Crest feature (Section 1.1) and the other (37–38°N, 15–17°E) with meanders of the AIS off the eastern coast of Sicily. For optimal sampling, these locations of high variability appear in most need of future temperature probe gathering.

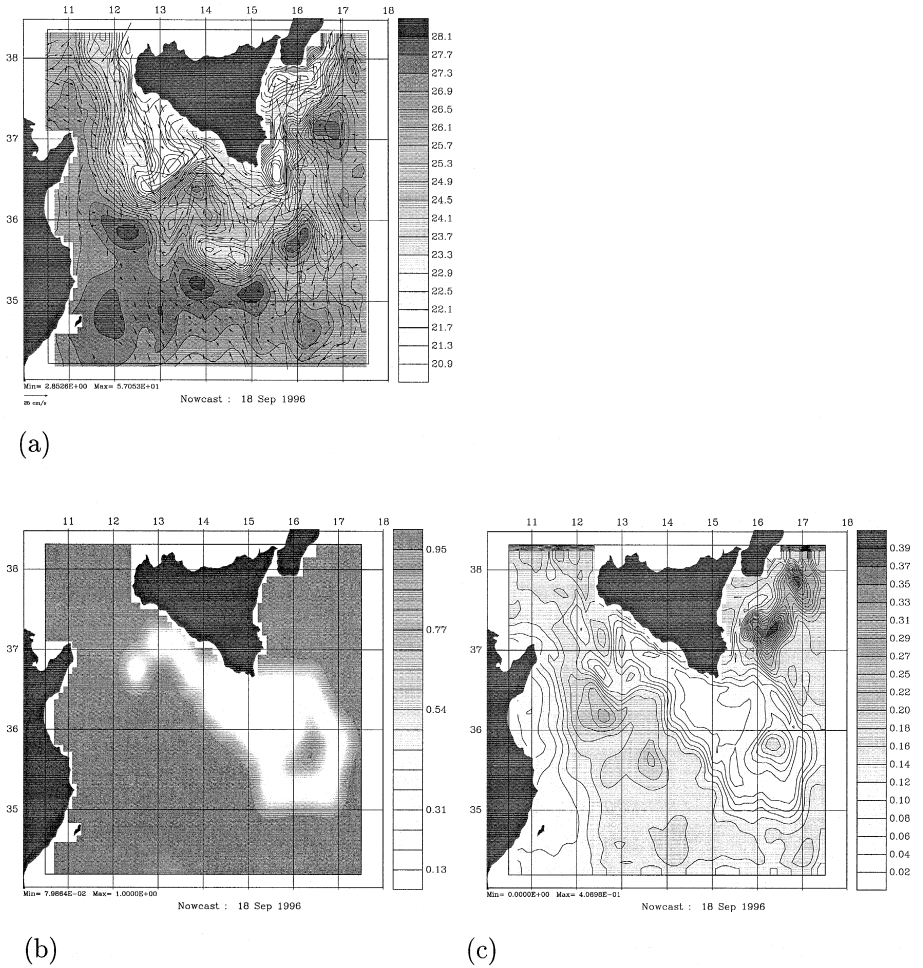

Fig. 1. (a) Surface temperature map (°C) for Sept. 18 after ESSE assimilation, overlaid with surface velocity vectors (scale arrow is 0.25 m/s); (b) Normalized expected error (0–1) of the surface temperature mapped from the new Sept. 18 observations; (c) Root mean square error (°C) of the estimate shown in (a). Before data assimilation the error range was ± 1.5°C. Real-time field and error forecasts were made at Harvard using ESSE with the data provided by Sellschopp et al., SACLANTCEN.

In general, such capabilities allow the use of optimization schemes to estimate data optimals, i.e., the time-variant sampling patterns and sensor types which maximize the decrease of errors. For more on such practical results and on the parameters of the real-time ESSE experiments (elapsed-times, parallel networking, dynamical and measurement models, etc), we refer to Lermusiaux (1997).

The present data-driven estimation in the Sicily Channel concentrate on RR96 between Sept. 15 and Sept. 24. The main purpose of this paper is to report the estimation and study of the physical fields and their dominant variability and error covariances.

Since this is a first endeavor with real data, some time is spend illustrating the estimation methodology. The scientific and technological results are discussed and studied along the way, as they are obtained. The advances made and the corresponding opportunities are summarized at the end. The presentation is intended to show that analyzing the evolution of the dominant decomposition of covariance matrices is very valuable for many reasons, ranging from the elucidation and modeling of real ocean processes to the efficient and objective design of observational strategies.

The organization of this paper is as follows. Section 1.1 briefly overviews the regional features and scales of variability. Section 2 deals with the estimation parameters. Section 3 describes and analyzes the results of the ten days of nonlinear estimation. The initialization of the error subspace is presented in Section 3.1. Several features associated with the dominant variability in the Strait during RR96 are identified. The estimation with predictions of the fields and dominant error covariances is studied in Section 3.2. The predictability error eigenvectors obtained are shown to be valuable for organizing and describing the variations of variability in the region. For quantitative and qualitative evaluations, intercomparisons with OI fields, clear SST images and available in situ data are carried out. Section 4 consists of a summary and conclusions. The Appendix defines the notation frequently used and overviews the machinery of the ESSE scheme employed.

1.1. Descriptive overview of the regional features and scales of variability

The Strait of Sicily (Fig. 2) separates the Western from the Eastern Mediterranean basins. The topography is complex, with the large and shallow Tunisian and Sicilian shelves (above 200 m) surrounding a narrow, double-sill trench (400 m) south of Malta Island, and a deeper basin (up to 1000 m) south of the Adventure Bank, between the Pantelleria and Malta Islands. Past the Ionian shelfbreak, the slope is steep, almost oriented north–south along 16E. This region is referred to as the Ionian slope.

A recent description of the general surface-intensified circulation in the Eastern Mediterranean and Strait of Sicily is given in Robinson et al. (1991). In the Sicily Channel, the fresh modified Atlantic water (MAW, in 1996, $\sim$37–37.8 PSU and $\sim$16–24°C) inflows in the surface layer ($\sim$0–150 m) from west to east, mainly by advection within the AIS. It was found during RR96 that within the Strait in summer conditions, the meanders of the AIS are mainly associated with surface thermal structures. As shown on Fig. 3, the free jet enters the Strait southward, along the western side of Sicily. It flows past Pantelleria on the north, bears northwestward around the Adventure Bank Vortex (ABV), then turns back southeastward in the Maltese Channel Crest (MCC), to go around the Ionian Shelf Break Vortex (IBV). These three features were subjectively identified during RR96 and named by Robinson et al. (1998b). Past the IBV, the AIS flows off the shelf into the upper western Ionian Sea, possibly bifurcating and breaking off into several streams. Interestingly, the present real-time study objectively confirms all of these independent findings. Another result is that two other features associated with the dominant variability are identified.

The main complement to the surface MAW exchange is the deep outflow, from east to west, of the salty modified Levantine intermediate water (MLIW). The MLIW (in

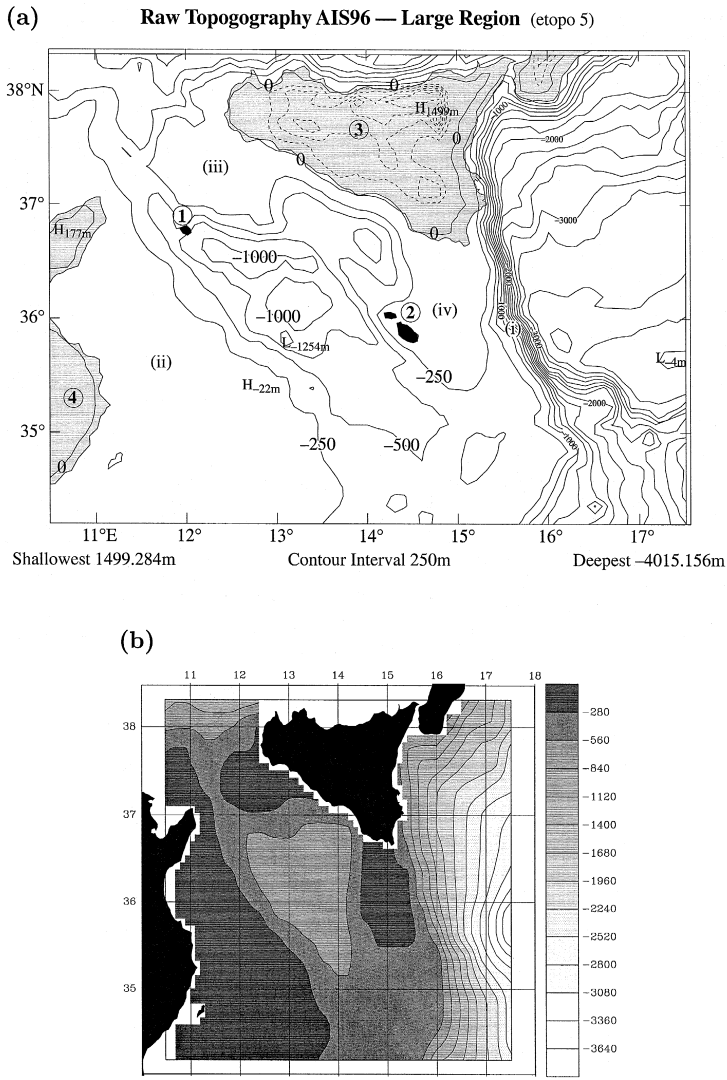

Fig. 2. Panel (a) shows the etopo5 topography of the region studied. The numbers indicate respectively, Pantelleria Island (1), Malta Island (2), Sicily (3) and Tunisia (4). The (i)'s indicate topographic features: the Ionian slope (i), Tunisian shelf (ii), Adventure Bank (iii) and Maltese plateau (iv). Panel (b) is the bottom topography at tracer grid points employed in the PE numerical model.

1996, ∼38.8 PSU and ∼14.2°C) enters the Channel usually within the sills south of Malta, and slowly flows out the Strait, into the western basin. The MLIW core is commonly found around 250–300 m. The present results confirm these facts and clearly indicate that the deep MLIW variability can influence the variability of the surface-intensified features.

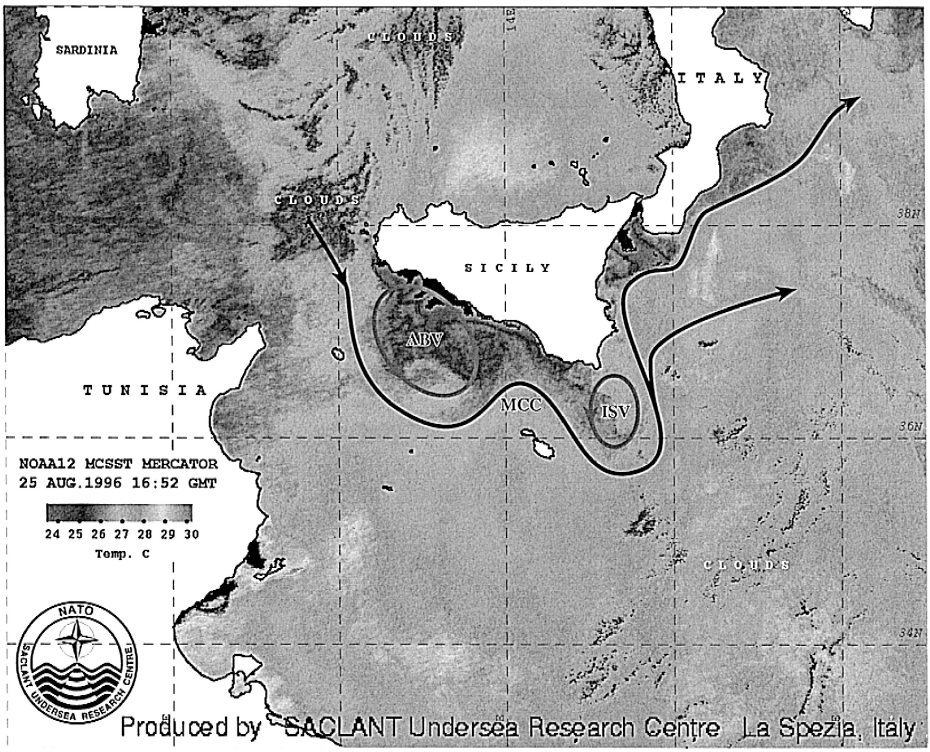

Fig. 3. Satellite SST distribution for August 25, 1996, with a cartoon of the summer surface circulation features identified during RR96 by Robinson et al. (1998b). The picture was downloaded from the real-time unclassified RR96 World Wide Web server of the SACLANTCEN.

The variability in the Strait occurs at several scales (Robinson et al., 1998b). The AIS interacts along its path with various energetic mesoscale events (e.g., eddy formation, filaments, unstable meanders), with time-scales of order of days (Moretti et al., 1993 and references therein). Weather patterns and associated winds can influence the internal dynamics, as exemplified by the cold upwellings along the southern coast of Sicily (Fig. 3). At higher frequencies, the gravity and Ionian shelf waves, the inertial component and tidal effects are important. Finally, mixing events between the double flow system occur, which has lead to defining multiple water masses (Warn-Varnas et al., 1998).

2. Estimation parameters

2.1. Data

The hydrographic observations collected from the beginning of RR96 until Sept. 15 are illustrated on Fig. 4a. This is the data set utilized to estimate the initial ocean fields and their error subspace on Sept. 15 (Sections 2.3 and 3.1). It contains 926 hydrographic

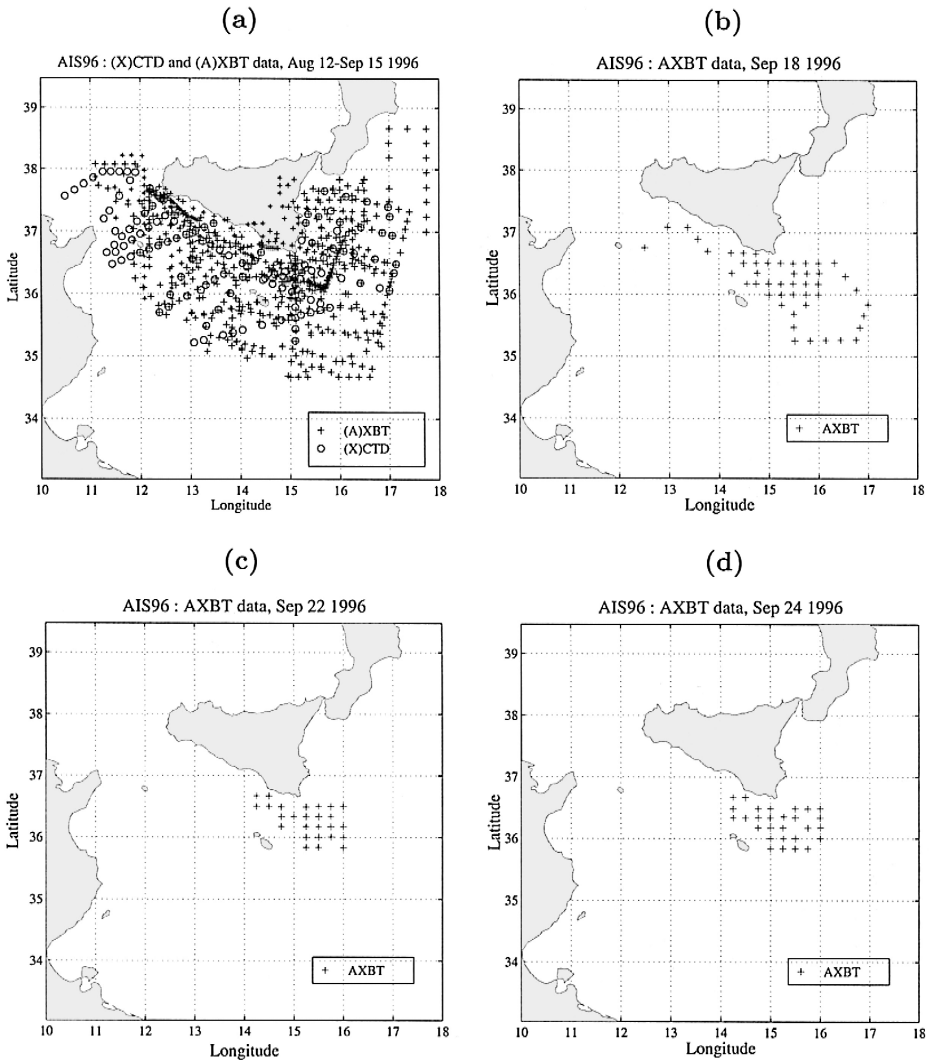

Fig. 4. Panel (a): Coordinates of hydrographic profiles collected during the period August 12–September 15, 1996 of the Operation Rapid Response 96. This is the data set employed in the initialization for Sept. 15, as provided by Sellschopp et al., SACLANTCEN. Panels (b–d): Coordinates of temperature vs. depth probes collected by three flights of a NAVOCEANO detachment. Panel (b) shows the probe locations for the flight of Sept. 18, Panel (c) for Sept. 22 and Panel (d) for Sept. 24, 1996. The sampling strategies on Sept. 22 and Sept. 24 were constrained by naval purposes.

profiles: 135 (X)CTDs and 791 (A)XBTs. The initial fields and errors are then evolved until Sept. 24, assimilating the subsequent observations as they become available (Section 3.2). Fig. 4b–d show the surface location of these new hydrographic probes. They consist of AXBT flights designed by Harvard and the SACLANT Center, using a

subjective adaptive sampling strategy (Robinson, personal communication). Presently, the flight of Sept. 18 and that of Sept. 22 are assimilated (Fig. 4b–c). The flight of Sept. 24 (Fig. 4d) is only utilized to evaluate the estimation methodology.

2.2. Dynamical model

The dynamical model is the nonlinear primitive equation (PE) model of HOPS (e.g., Robinson, 1996), in its rigid-lid configuration. The state variables are the (dynamical) tracers, the temperature T and salinity S, the barotropic transport stream function ψ, and the zonal (x) and meridional (y) internal velocities, $\hat{u}$ and $\hat{v}$, respectively (see Appendix A for notations). External velocities are obtained from $\bar{u} = -\nabla_h \wedge \psi e_z / H$, where the operator $\nabla_h \wedge (\cdot)$ is the horizontal curl, e_z the vertical and H the local depth. The values of the numerical and physical parameters used in this study are listed in Table 1. The horizontal resolution is 9 km. The domain extension is 630 km in the zonal and 459 km in the meridional direction, respectively (Fig. 2). In the vertical (z), 20 levels are distributed based on a ''double sigma'' transformation (Lozano et al., 1994; Sloan, 1996). This is a piecewise linear transformation which uses two ''topography-following'' sigma systems: one from the surface to an intermediate depth $h_c(x, y)$, the other from h_c to the bottom. For suitably chosen h_c, this maintains relatively flat levels above h_c in both the shelf and deep ocean. The dimension of the state vector is 299,052. The time step was bracketed to 450 s.

Horizontally, the parameterization of the subgrid-scale mixing processes and filtering of numerical noise is based on a Shapiro filter (Shapiro, 1970). Its parameters are the order p, number q of application per time step and number r of time steps in between applications. For each state variable (Table 1), the values p, q, r were determined based on curves of effective diffusivity as a function of horizontal-scales, and on a compromise between smoothing computational noise and allowing physical instabilities to occur (Lermusiaux, 1997). The vertical mixing is a Laplacian mixing, with fixed eddy

Table 1
Dynamical model parameters

Numerical Parameters	Centroid latitude and longitude	36.25°N, 14°W
	Domain extension	630 km (x), 459 km (y)
	Grid resolution	9 km
	Grid size	71 (x), 52 (y), 20 (levels, double sigma)
	Time step	450 s
	State vector size	$n = 299{,}052$
Physical Parameters	Shapiro filter	F_u, F_v: 1611; F_T, F_S: 411; $F_{\bar{\omega}_t}$: 211
	Open bond condition	$\hat{u}$,$\hat{v}$: (ORI); T, S: (ORI); ψ: ($\mathrm{ORE}_{1/2}$); $\bar{\omega}_t$: ($\mathrm{ORE}_{1/2}$)
	Vertical mixing	$A_v = 0.5\ \mathrm{cm^2\ s^{-1}}$, $A_v^{evet} = 50\ \mathrm{cm^2\ s^{-1}}$ $K_v = 0.1\ \mathrm{cm^2\ s^{-1}}$, $K_v^{evet} = 50\ \mathrm{cm^2\ s^{-1}}$
	Drag coefficient	$C_d = 2.5 \times 10^{-3}$
	Rayleigh coastal friction	$\tau_c = 7200$ s, $L_c = 9$ km
	Rayleigh bottom friction	$\tau_b = 3600$ s, $H_b = 2$ bottom levels, with $H_b \leq 50$ m

viscosity $A_v = 0.5$ cm^2 s^{-1} and diffusivity $K_v = 0.1$ cm^2 s^{-1}. Convective adjustment is utilized when the water column is statically unstable, with a vertical viscosity A_v^{cvct} and diffusivity K_v^{cvct} both equal to 50 cm^2 s^{-1}. At the open boundaries (Lermusiaux, 1997), Orlanski radiation (ORI/ORE) conditions (Orlanski, 1976) were preferred for all variables. Across coastlines, the normal flow and tracer flux are set to zero. Along coastlines, the tangential flow is slowed down at the coast, using a Rayleigh friction of relaxation time $\tau_c = 7200$ s and Gaussian decay horizontal-scale of one grid point, $L_c = 9$ km. This condition is a ''damped free-slip''. At the bottom, a dynamic stress balance is applied to the momentum equations, with a drag coefficient $C_d = 2.5 \times 10^{-3}$. An additional Rayleigh bottom friction is employed to control possible numerical error growth in the barotropic transport and parameterize a simple bottom boundary layer for momentum. Its parameters are a relaxation time τ_b of 3600 s and Gaussian decay vertical-scale H_b of two bottom levels, with $H_b \leq 50$ m. Although atmospheric forcings were used in operations, during the period considered here, they are not the main source of variability. For simplicity, the wind-stress and surface buoyancy flux are thus set to zero; the internal dynamics is the main interest.

2.3. Field initial conditions

The gridded fields are initialized by objective analysis (OA) and PE adjustment, using the data gathered up to Sept. 15 (Fig. 4a). For better stability and accuracy of the initial fields, the salinities of the AXBTs are estimated. In the Strait of Sicily, this is challenging because there is no clear T/S relationship and the T/S distribution varies in all dimensions (x, y, z, t). All of the procedures investigated employed the available CTD data (Fig. 4a) as a pool of reference T/S profiles. The method selected (e.g., Lermusiaux, 1997) computes the salinity of a given AXBT using a weighted average of the reference salinities. The weights in the average increase with the similarity between the location, profile shape, depth and temperature range of the AXBT data and reference T data. Constraints based on the reference T/S diagram are also imposed. The resulting 926 T/S profiles are first gridded on flat levels using a two-scale horizontal OA. The first stage maps the large-scales (subbasin-scale) tracer fields, the second adds the mesoscale correction to the subbasinscale estimates. The associated error correlation is the second derivative of an isotropic Gaussian. It has been commonly used in the Mediterranean (e.g., Robinson and Malanotte-Rizzoli, 1993). The measurement error covariance matrices are assumed diagonal, with constant non-dimensional variance. Table 2 summarizes the main parameters.

A first-guess at the initial flow conditions is computed assuming geostrophic balance, with a level of no motion at 180 m. The nonlinear momentum equations are then integrated from this first-guess, keeping the objectively analyzed temperature and salinity fixed. This integration is usually continued until the mean kinetic energy stabilizes around a plateau, without rapid changes. This procedure is called an *adjustment PE integration* and the resulting initial fields are said *PE-adjusted*. The adjustments at play are, in order of importance: (i) the generation of the deviation between the inviscid, linear, depth-integrated PE flow and the first-guess, depth-integrated flow in geostrophic balance from a flat level of no motion, here at 180 m. This process is a joint

Table 2
Parameters of the tracer objective analyses

Horizontal grid resolution	9 km
18 flat levels	0.5, 15, 30, 45, 60, 90, 120, 170, 220, 270, 320, 750, 1400, 1600, 1800, 2000, 2250, 4000 m
Subbasin-scale zero-crossings	400 km
Subbasin-scale decorrelation scale	150 km
Mesoscale zero-crossings	50 km
Mesoscale decorrelation scale	30 km
Mesoscale time decorrelation	3 days
Subbasin-scale (historical) data error variance	0.2 (non-dimensionalized within 0 to 1)
Mesoscale (synoptic) data error variance	0.1 (non-dimensionalized within 0 to 1)

effect of baroclinicity and relief, which, by conservation of mass, induces vertical velocity adjustments at depths. As pointed out by Cane et al. (1998) and anticipated by Mertz and Wright (1992), it should not be understood in the sense of the classic ''JEBAR term'', which does not account for all topographic effects; (ii) the diffusion of momentum (surface and bottom diffusions, coastal stresses, eddy viscosities), in accord with the specifics of the fixed density field. This process includes the fast adjustment (days) to a momentum bottom boundary layer model (MacCready and Rhines, 1993), which here dominates the slow (years) pressure compensation of Mellor and Wang (1996) since the first-guess geostrophic velocities are already small at depths; and finally, (iii) the adjustment of the momentum nonlinearities. The adjustment PE integration is not a search for a steady state. It is only analogous to a ''Picard integration'' (Garabedian, 1964) in the sense that it reduces the time-rates-of-change towards values acceptable for a smooth, but high Reynolds number, PE dynamical regime.

The initial PE adjusted velocities and corresponding objectively analyzed tracers, are shown on Fig. 5. One recognizes the features described in Section 1.1. The AIS is clearly visible on the total velocity map, with several meanders and mesoscale eddies along its path, e.g. two cold eddies starting to pinch off the IBV. The PE adjusted barotropic transport through the Strait on Sept. 15 is estimated to about 0.7 Sv. The dominant uncertainties of these fields, in part due to data errors and environmental noise, are estimated in Section 3.1.

2.4. Assimilation scheme

In this study, the Bayesian approach is approximated by minimum error variance principles. To carry out the data-driven forecasts in real-time, filtering problems are solved: data are melded with the forecast as they become available, without correcting past estimates based on future observations. The AXBT data with estimated salinity (Sections 2.1 and 2.3) are assimilated once, on the day they are observed. The present ESSE scheme and its parameters are presented in Section 2.4.1. To evaluate or benchmark the ESSE fields, an OI scheme is utilized. It is described in Section 2.4.2. For recent comprehensive data assimilation treatises, we refer to Daley (1991), Ghil and Malanotte-Rizzoli (1991), Bennett (1992), Sundqvist (1993), Evensen (1994), Cohn and Todling (1996), Malanotte-Rizzoli (1996), Wunsch (1997) and Robinson et al. (1998a).

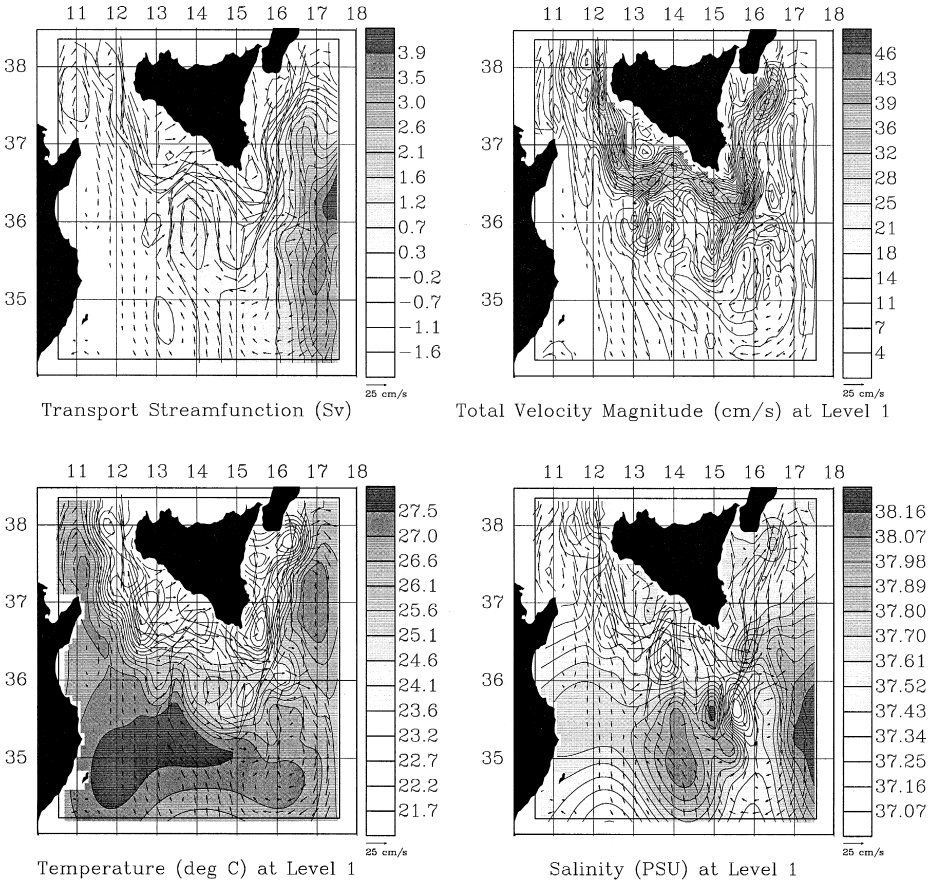

Fig. 5. Surface initial conditions for September 15, 1996. The salinity and temperature fields are obtained by objective analysis. The internal velocity and barotropic transport stream function are computed by adjustment PE integrations starting from velocities in geostrophic balance.

2.4.1. ESSE scheme

The present estimation approach reduces the error statistics to multivariate, time-variant error subspaces (ESs). Its geophysical motivations and rationale are given in (Lermusiaux, 1997) and (Lermusiaux and Robinson, 1998). In the minimum error variance context, the consistent ESs are characterized by the dominant eigendecompositions of error covariance matrices, or in other words, by dominant error empirical orthogonal functions (EOFs) and coefficients. At assimilation times, the data and forecast are then combined by minimizing the a posteriori variance in the ES forecast, in accord with the full dynamics and past measurements, and their respective dominant uncertainties. The four-step algorithm employed to carry out this estimation is summarized in Appendix A. The parameters of the melding (measurement model), adaptive error learning and forecast steps are given next. The ES initialization is described later in Section 3.1.

2.4.1.1. Measurement model parameters. The measurement model parameters (Section A.2) are the operator **C** and error covariance matrix **R**. Presently, the T/S profiles are first mapped onto the PE model levels by vertical linear interpolation. The matrix **C** then bilinearly interpolates the tracer forecast onto these profile-level intersections, or so-called data-points. The measurement error co-variance matrix $\mathbf{R} = [r_{ij}]$ is assumed diagonal, of elements r_{ii} a function of the internal dynamics, with a time and depth dependent amplitude:

$$r_{ii}^{\upsilon}(z,t) = \sigma^{\upsilon^2}(t) + \epsilon^{\upsilon}(t)\,\sigma_r^{\upsilon^2}(z,t), \tag{1}$$

where the superscript υ specifies the measured variable, t is the time and z the vertical coordinate. In Eq. (1), r_{ii}^{υ} is assumed to consist of two uncorrelated components: σ^{υ^2}, which accounts for the precision of the sensor utilized, human errors and forward interpolation errors; and the environmental noise, here estimated by $\epsilon^{\upsilon}\,\sigma_{\mathrm{r}}^{\upsilon^2}$, where $\sigma_{\mathrm{r}}^{\upsilon^2}$ is the internal, residual variability variance of the field υ and ϵ^{υ} is a factor to scale noise variances. The present values of σ^{υ} were estimated to 0.03°C for T profiles and to 0.01 PSU for S profiles. The comprehensive computation of the environmental noise is challenging. It often involves the estimation of the internal wave field and sub-mesoscale phenomena (Turner, 1981; Munk, 1981) from larger scale data (e.g. Flierl and Robinson, 1977). Several approaches for estimating $\sigma_{\mathrm{r}}^{\upsilon^2}(z,t)$ of the 20–35 km resolution data (Fig. 4b–d) were tested, but the model chosen is still a simple one. For initial conditions, $\sigma_{\mathrm{r}}^{\upsilon^2}(z,0)$ at a given depth is set to the horizontal average of the square of the differences, $\mathbf{d}_{\mathrm{his}} - C\hat{\psi}_0$, between the historical data ($\mathbf{d}^{\mathrm{his}}$, Fig. 4a) and initial conditions ($\hat{\psi}_0$, Fig. 5). The evolution of $\sigma_{\mathrm{r}}^{\upsilon^2}(z,t)$ is estimated as follows. At melding time, $\sigma_{\mathrm{r}}^{\upsilon^2}$ at a given depth is set to the horizontal average of the variance at data-points of the ensemble forecasts with respect to the data to be assimilated. Simply assuming proportionality with this variability, $\epsilon^{\upsilon}\,\sigma_{\mathrm{r}}^{\upsilon^2}(z,t)$ is then an approximate forecast of the environmental noise. The values of ϵ^{υ} were set to 0.25 for $\upsilon = T$ and to 0.3 for $\upsilon = S$. This quantitative scheme for forecasting the environmental noise led to robust assimilations. From our sensitivity studies, models like Eq. (1) play an important role. For example, if the estimated (environmental) data error variance is too small or of erroneous distribution, scales that are not of interest can spoil the state estimate. Further theoretical and observational research is required for more advanced formulations.

2.4.1.2. Adaptive ES learning parameters. The present scheme is adaptive (Section A.3): the possibly significant a posteriori data residuals are employed to correct (learn) the ES. These residuals are first objectively analyzed and then used to update the a posteriori ES. The main parameters in the ES learning pertain to the mapping of the residuals. This mapping is carried out here by a multivariate ESSE analysis (Lermusiaux et al., 1998), assuming that the background error covariance function is separable in the horizontal and vertical. From Kronecker product properties (Graham, 1981), the dominant eigendecomposition of the background error covariance matrix is then obtained from the these of the horizontal and vertical error covariance matrices. In the horizontal, the covariance function is assumed isotropic mesoscale (Section 2.3), of decorrelation scales set to 25 km, and zero-crossings to 50 km. In the vertical, the eigendecomposition is estimated from the vertical EOFs of the residuals.

2.4.1.3. ESSE forecast parameters. The forecast of the state and ES characteristics is here based on a Monte Carlo ensemble approach (Section A.4). Several choices of state and ES estimates are possible. In this study, the state forecast is the central nonlinear forecast. The ES forecast is obtained as follows. An ensemble of perturbed states is created such that, at the infinite ensemble limit, the sample covariance matrix from the a posteriori the $\hat{\psi}_{k+1}(+)$ tends to the a posteriori error subspace covariance matrix. The signs of the perturbations are constrained by data to avoid states of adequate variance, but of possibly too unrealistic physics. Model errors are assumed null and the PE stochastic forcing (Lermusiaux, 1997) set to zero. While batches of forecasts are computed in parallel, a similarity coefficient measures the added value of new integrations to assess the convergence of the ES forecast. When the coefficient is large enough, parallel iterations are stopped. The size of the ES hence evolves with time, in accord with data and dynamics.

2.4.2. Optimal interpolation scheme

The OI consists of a two-scale OA of the new data, followed by a blending of the forecast and OA fields. It is a robust scheme, with successes in several regions of the world's ocean (Lozano et al., 1996; Robinson et al., 1996). Presently, the profiles (Fig. 4b–c) are first gridded in a two-scale (subbasin-scale, mesoscale) minimum error variance estimation. These analyses are carried out using the parameters of Table 2. Gridded velocities are obtained assuming geostrophic balance with the analyzed density field, for a level of no motion at 180 m. The analyzed tracers and internal flow are then blended with the forecasts. [1] The weights in the blending are such that where the error variance of the gridded data is one, the forecast weight is null, and inversely (Robinson, 1996). With this OI, the external flow adapts to the new data after the blending, by dynamical adjustments.

3. Data-driven fields and covariances

The present nonlinear estimation starts on Sept. 15 and ends on Sept. 24, using the parameters of Section 2. The initialization of the ES which leads to an interesting decomposition of the summer variability is described in Section 3.1. The subsequent ten days of field and dominant error covariance estimates are studied and evaluated in Section 3.2.

3.1. Error subspace initial conditions

For the limited number of comprehensive modeling efforts in the Strait of Sicily, simple principles are used to initialize the ES on Sept. 15. As for the initial fields $\hat{\psi}_0$ (Section 2.3), the main information consists of the initial data (Section 2.1) and PE model (Section 2.2). The largest uncertainties of $\hat{\psi}_0$ are hypothesized to be generic mesoscale PE variability (features of about 15–100 km horizontal-scale or

[1] In future studies, the OA transport could perhaps be assimilated if its values in data regions were PE adjusted, in a fashion similar to that discussed in Section 2.3.

wavelength$/2\pi$). The corresponding variability subspace is thus estimated for the domain of main interest (sampled region on Fig. 4). The details of the algorithm are in Section A.1. Briefly, the eigendecomposition of the variability covariance matrix of the observed variables (here T/S) is first specified based on the initial data (Section 3.1.1). The dominant covariance matrix of the complete PE variability is then estimated by cross-covariances (Section 3.1.2): the initial fields $\hat{\psi}_0$ are perturbed based on the dominant T/S variability and the corresponding flow variability is build using an ensemble of nonlinear adjustment PE integrations (Section 2.3). The resulting PE variability from $\hat{\psi}_0$ is decomposed by SVD and scaled for adequate initial error variances.

3.1.1. Dominant eigendecomposition of the three-dimensional tracer error covariance matrix

The initial tracer variability covariance function is assumed separable in the horizontal and vertical. The covariance matrix is then amenable to exact eigendecomposition using Kronecker product properties (Graham, 1981). In the horizontal, the correlation function used (Section 2.3) has isotropic decorrelation scales set to 25 km and zero-crossings to 50 km. The eigendecomposition is simply carried out. In the vertical, the decomposition of the covariance matrix is estimated from the EOFs of the differences between the profiles available on Sept. 15 (Fig. 4a) and the initial tracer fields.

Fig. 6 illustrates the results of the vertical multivariate EOF decomposition. The normalized cumulative variance and four dominant EOFs are shown. These four EOFs explain 81% of the variance of the data residuals from the initial tracers (Fig. 5). The first EOF (32% of the variance) is surface-intensified. It mainly represents the temperature variability within the surface thermocline. The non-dimensional S in that first EOF is 4 times smaller in amplitude, but extends deeper, than T and has a secondary maximum around 200–400 m, locations of the MLIW. The second EOF accounts for 30% of the variance. It is mainly a salinity EOF. The signature in S is also deeper than that in T of EOF 1. Since the MAW is almost always found above 200 m depth, this signature in S is mainly related to Tunisian shelf and Ionian waters found in the eastern and southern part of the domain (Fig. 5). Hence, EOFs 1 and 2 likely correspond to two different water masses. The EOF 3 (12% of the variance) represents thermocline and halocline variabilities. Both T and S are mid-depth intensified, with one significant zero-crossing. The amplitudes in the surface layers are vertically uniform and about three times smaller than the mid-depths maxima. The T peak is within 20 to 100 m (thermocline depths) while the S peak is within 70 to 400 m (mainly halocline depths). Comparing the non-dimensional amplitudes of T and S, that of S is twice as large. During the months considered, the salinity variability associated with the MLIW and with the Tunisian shelf and Ionian waters is important for determining the local halocline/thermocline depths. Finally, the fourth EOF explains 7% of the variance. It has a structure opposite to that of EOF 3. However, the T/S amplitude ratio of EOF 4 is larger than the S/T ratio of EOF 3. The EOF 4 could thus be mainly temperature-driven processes, with no physical relation to EOF 3.

Combining the vertical and horizontal (not shown) decompositions (Section A.1, Eqs. (A5), (A6), (A7), (A8), (A9), (A10) and (A11)), the dominant eigendecomposition of the

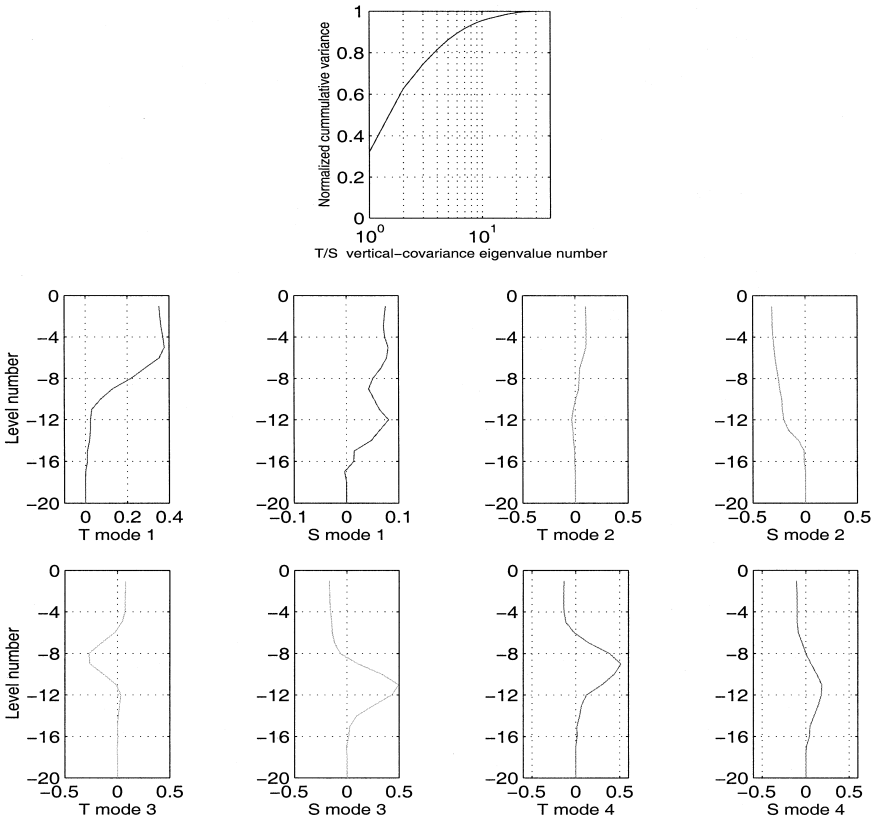

Fig. 6. Eigendecomposition of the non-dimensional covariance of the initial profile residuals, i.e., of the differences between the profiles available on Sept. 15 (Fig. 4a) and the initial T, S fields (Fig. 5). The top panel shows the normalized cumulative variance as a function of the eigenvalue number. The covariance $\mathbf{C}^{z}_{\mathrm{trc}}$ is $[40\times40]$. The first T, S vertical EOF explains 32% of the variance, the second 30%, the third 12% and the fourth 7%. These top four EOFs are plotted below, as a function of the level numbers. They are described in the text. They account for 81% of the variance, the top 18 EOFs for 99%.

tracer variability covariance $\mathbf{E}_{\mathrm{trc}}\,\Pi_{\mathrm{trc}}\mathbf{E}^{T}_{\mathrm{trc}}$ is obtained. Several of the dominant 3D eigenvectors or modes, columns of $\mathbf{E}_{\mathrm{trc}}$, are illustrated by Fig. 7. At a given depth, the non-dimensional amplitudes and signs of the T, S anomalies depend on the specific horizontal/vertical combination. The modes 1 to 10 are Kronecker products of the first vertical EOF (Fig. 6) with the dominant horizontal eigenvectors 1 to 10, respectively. The associated T and S anomalies are therefore in phase (partial compensating effects in density). However, modes 11 and 12 illustrated on Fig. 7 correspond to Kronecker products of the second vertical EOF with the two dominant horizontal vectors (not shown): the T and S surface anomalies are then in opposition. As plotted on Fig. 7, it is extremely encouraging that the three dominant modes of 3D tracer variability correspond to the dominant features subjectively, but independently, identified by Robinson et al. (1998b): mode 1 correspond to the Adventure Bank Vortex (ABV), mode 2 to the

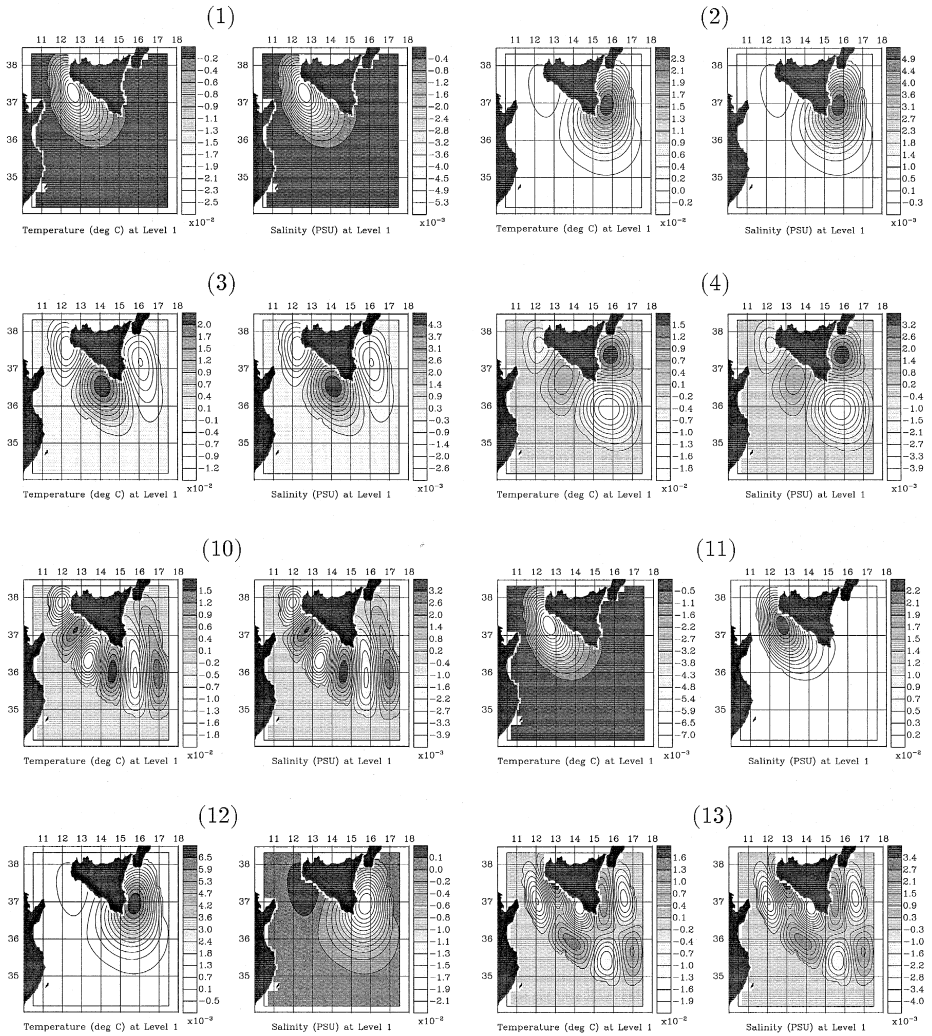

Fig. 7. Dominant eigenvectors of the normalized 3D mesoscale tracer variability covariance (limited to the sampled domain). Only the surface values are shown; they are discussed in the text. The isotropic horizontal zero-crossing is 50 km and decay scale 25 km. The size of the covariance is [147,680 × 147,680]. The Panel number indicates the mode number.

Ionian Shelf Break Vortex (IBV) and mode 3 to the Maltese Channel Crest (MCC), coupling the other two vortices. These features are in accord with the squeezing and stretching of the AIS over the local topography (Fig. 2), as was also addressed by Onken and Sellschopp (1998). The mode 4 identifies another feature at the entrance of the Strait of Messina. We name this vortex the Strait of Messian Vortex (SMV). As for the three other features (Robinson et al., 1998b), satellite SST images and associated wind data

(not shown) indicate that the SMV often corresponds to cold upwelled MAW. However, it does not maintain its structure during RR96 as strongly as the other three vortices. Meandering southward shelf currents on its western side (Böhm et al., 1987) and the lack of topographic controls on its eastern side are probable explanation.

These four identifications illustrate the potentials of ESSE for quantitative three-dimensional and multivariate variability studies. In the present situation, the specifics of the geometry and horizontal covariances were such that the orthogonality constraint did not significantly alter the dominant physical patterns. In other cases, one may need subsequent analyses (e.g., factor or cluster analysis) to disentangle the physics from of the dominant decomposition. In addition, the three-dimensional multivariate variability of a feature often corresponds to groups of eigenvectors. For example, the three-dimensional modes 11 and 12 of Fig. 7 correspond to the ABV and IBV as modes 1 and 2 did, but they mainly account for salinity dominated variabilities (Fig. 6). From our experience, the number of modes required is often of the order of the product of numbers required for horizontal and vertical univariate EOFs. For example, the present 400 dominant modes explain 68.2% of the total 3D tracer variance; the 1000 dominant explain 87% of the variance. In passing, these numbers account for all possible realizations of the 3D mesoscale tracer variability. Because of the memory in time, only a portion of these eigenvectors is active at a given instant (e.g., mesoscale eddies are not everywhere at the same time).

3.1.2. Dominant eigendecomposition of the three-dimensional PE error covariance matrix

As outlined in Section A.1 (Eqs. (A12) and (A13)), the velocity responses corresponding to the dominant 3D tracer eigenmodes (Section 3.1.1) are computed first. Each tracer mode is dimensionalized and added to the initial tracer fields $\hat{\psi}_{\text{trc}}$. The resulting ensemble of unbalanced fields is adjusted by integrating the momentum equations for 2 model-days, keeping T and S fixed. Fig. 8 illustrates the velocity responses of these adjustment PE integrations (Section 2.3). The dimensional difference fields shown correspond to the tracer modes 1 to 4, and 10 to 13, that were plotted on Fig. 7. The specifics of the state $\hat{\psi}_0$ (e.g., density features) and topography (e.g., Ionian slope and basin between Pantelleria and Malta) strongly influence the flow responses to tracer perturbations. The barotropic transport responses usually have their largest amplitudes and gradients along the deep eastern side of the Ionian shelfbreak (e.g., compare Panels 1 and 11 with the others). The internal velocity anomalies of Panels (1–4) explain internal circulation variabilities corresponding to the largest-scales of the ABV, IBV, MCC and SMV, respectively. The internal velocity responses to tracer modes of shorter horizontal scales (e.g., Panels 10 and 13) clearly show that they are mainly subject to geostrophic constraints (the meridional internal velocity is not shown for this reason). The effects of the vertical tracer decomposition (Fig. 6) are also observed. The barotropic transport and internal velocity responses of Panels 11–12, which correspond to the second vertical tracer EOF (T and S in opposition, S dominating), differ from that of Panels 1–2, which correspond to the first vertical tracer EOF (T and S in phase, T dominating). This difference is especially striking for the transport responses, which adjust via baroclinicity, relief, diffusion and nonlinear effects (Section 2.3).

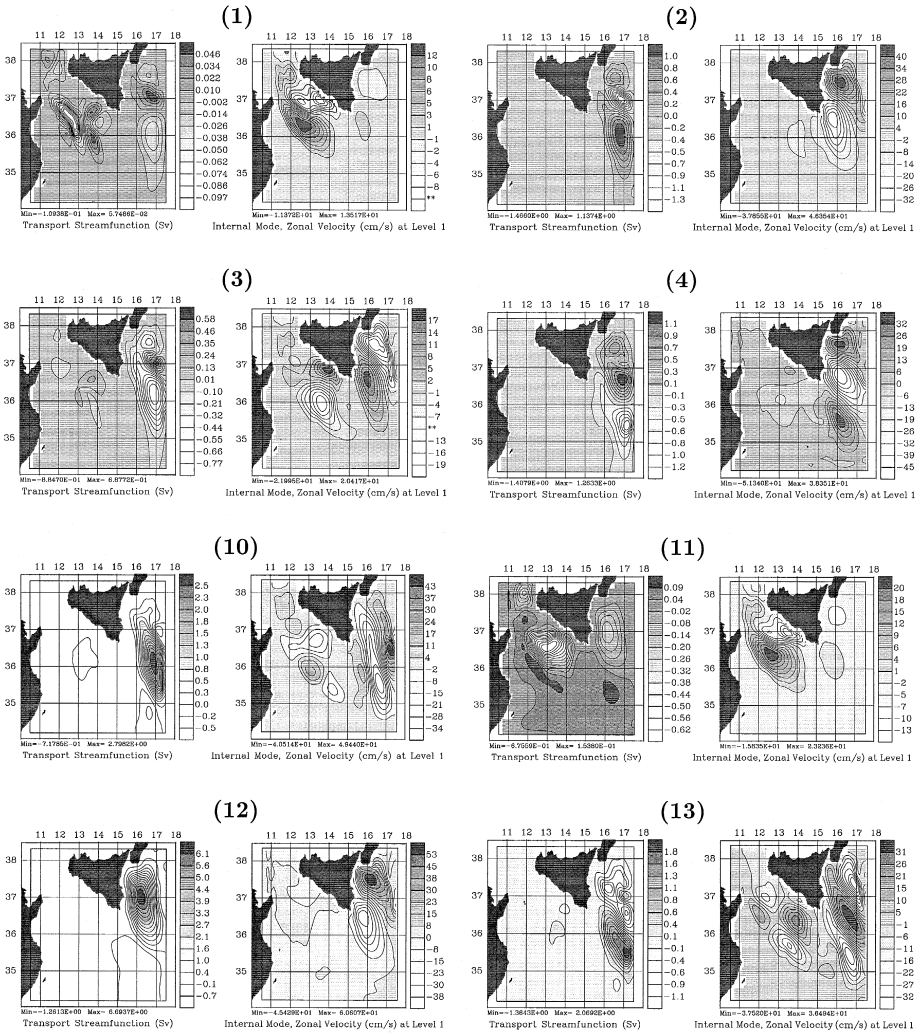

Fig. 8. Dimensional, PE adjusted velocity responses corresponding to the 3D mesoscale tracer variability eigenvectors (1) to (4), and (10) to (13), illustrated in Fig. 7. The Panel numbers indicate these 3D tracer eigenmode numbers. Two response fields are shown for each mode: the barotropic transport stream function and the internal zonal velocity. They are discussed in the text.

As the adjustment PE integrations for velocity responses are carried out in parallel, the SVD of the matrix which columns are the normalized differences between the PE adjusted states and initial state is updated and a convergence criterion evaluated (Section A.1, Eqs. (A13), (A14) and (A15)). The criterion measures the value added by new differences. In the present case, a similarity coefficient is required to be larger than 97%. This is satisfied after 289 integrations (Lermusiaux, 1997). The corresponding SVD estimates the dominant decomposition of the initial PE variability covariance matrix.

The 50 (150) dominant left singular vectors are found to explain 55% (84%) of the variability variance explained by the 289 vectors. Figs. 9–11 illustrate a few of these vectors. In passing, they did not vary significantly with the open-boundary conditions chosen (Section 2.2).

Fig. 9 shows the two dominant vectors of PE variability for Sept. 15. Panels 1a–2a are horizontal maps of ψ, surface T, S and $\hat{u}$. Panels 1b–2b are vertical cross-sections of T, S, $\hat{u}$ and $\hat{v}$ along the axis 17E of large amplitudes. The first two vectors are almost in quadrature of phase in the horizontal and are associated with baroclinic/barotropic

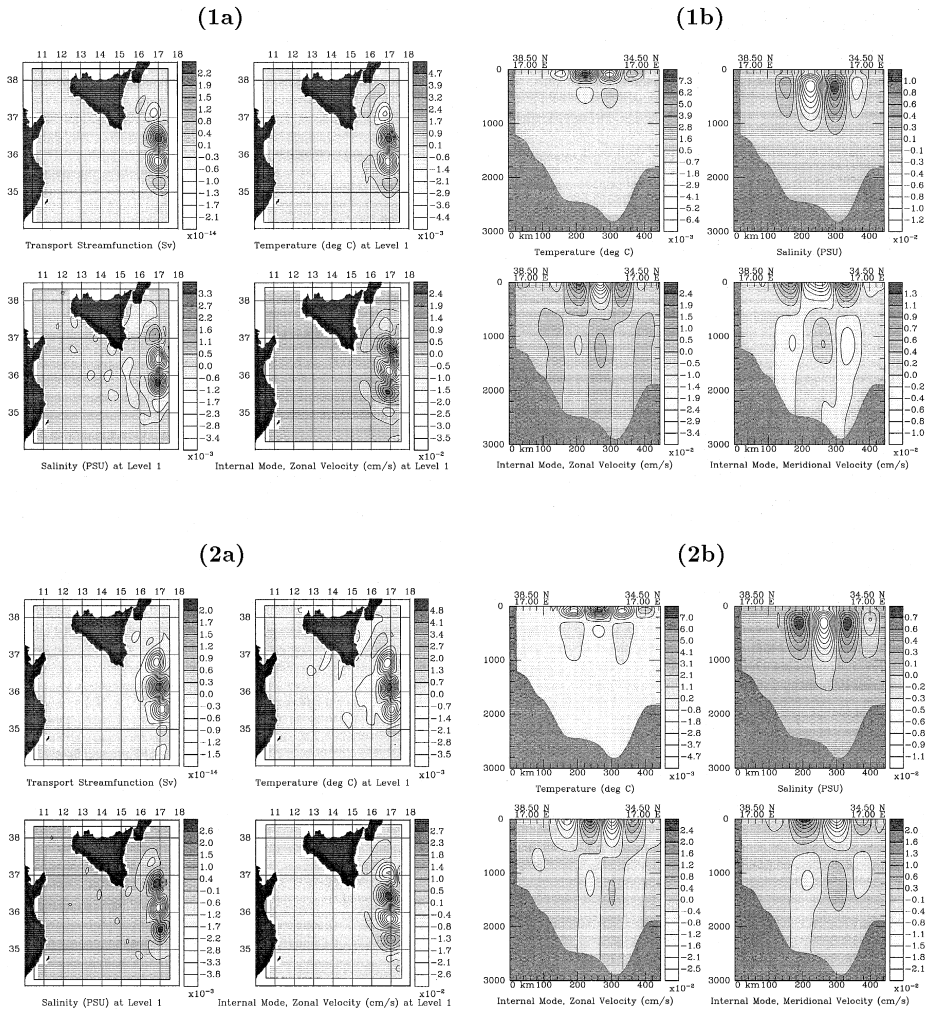

Fig. 9. Multivariate eigenvectors of the normalized, **PE** adjusted, initial (Sept. 15) error covariance estimate. The vectors illustrated are the two dominant modes of the estimated PE variability for Sep. 15. The covariance is [299,052 × 299,052]. The Panel numbers indicate vector numbers, with index *a* for the first level, and *b* for a vertical cross-section along 17E.

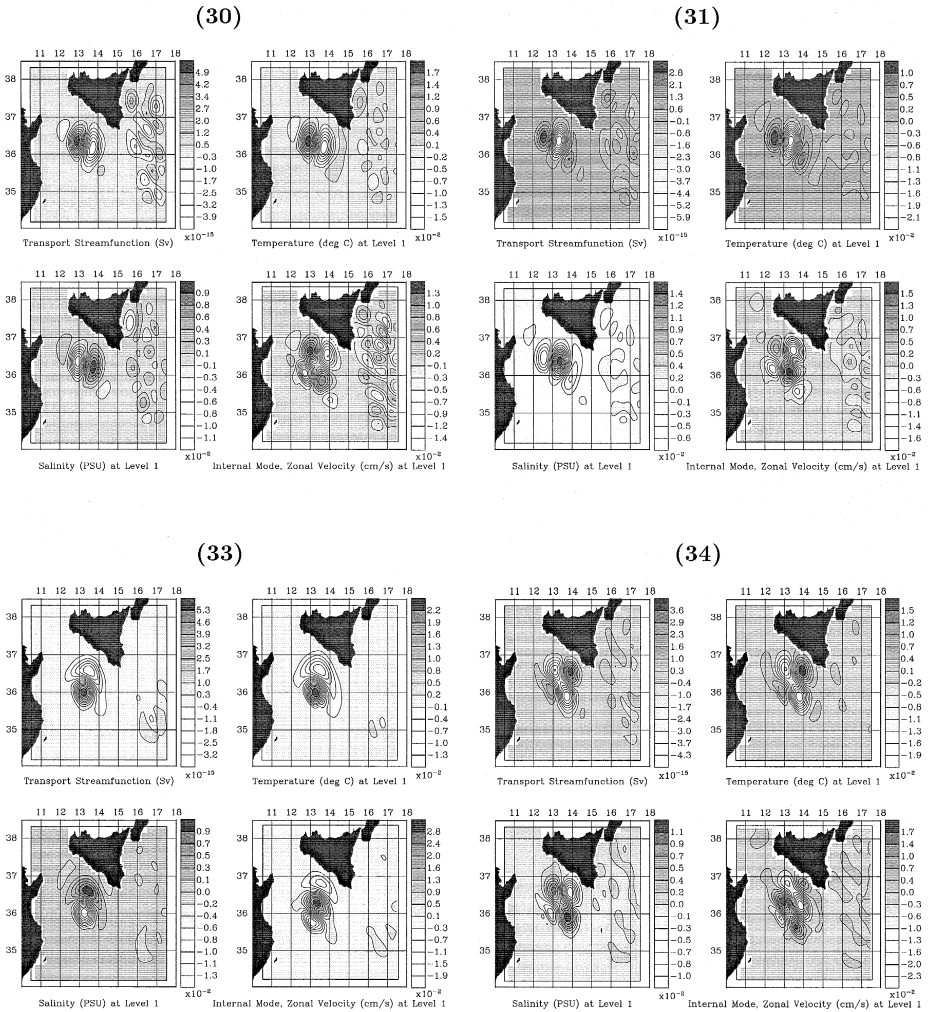

Fig. 10. As for Fig. 9, but for the surface values of eigenvectors (30, 31, 33, 34). The variables shown are indicated by the bottom titles. These four vectors are associated with the dominant internal variability of the Adventure Bank Vortex and Maltese Channel Crest.

topographic Rossby wave patterns propagating along the steep Ionian slope (Fig. 2). Their dominant wavelength is about 120 km. The maps (1a–2a) show that in the surface, both vectors-are dominated by their total velocity anomalies. [2] The non-dimensional surface tracer anomalies are almost one order of magnitude less. The cross-sections (1b–2b) show maxima for temperature within 20 to 70 m, depths of the MAW

[2] In the normalization (Appendix A), amplitudes are divided by the number of vectors (289), hence leading to magnitudes of order 10^{-2}, for T, S, $\hat{u}$ and $\hat{v}$ fields, and 10^{-14} for ψ (the 10^{12} arises from Sv units).

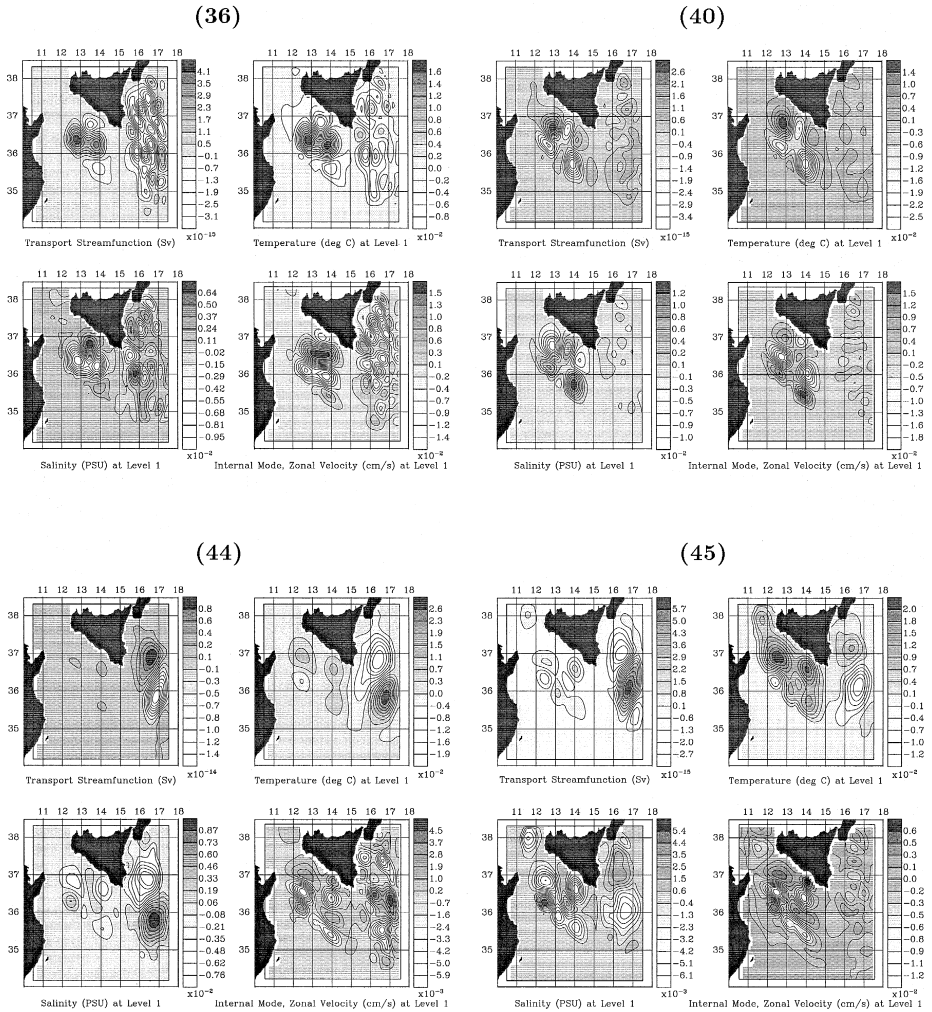

Fig. 11. As for Fig. 9, but for the surface values of eigenvectors (36, 40, 44, 45). The variables shown are indicated by the bottom titles. These four vectors account for eventual couplings between Ionian slope processes and phenomena of the Pantelleria and Malta Islands basin.

variability along the slope, and for salinity within 200 to 500 m, depths of the MLIW variability along the slope. The tracer perturbations are mainly limited to these depths. For both vectors, T and S in the surface layer have opposite horizontal phases, with similar normalized amplitudes, hence adding effects on the density anomaly. The internal velocity signature is close to thermal-wind balance. It is mainly limited to the surface 500 m, with a small amplitude first-baroclinic mode structure below. At depths, the barotropic transport anomaly is the dominant field. This indicates that barotropic current data should be most useful in this region. The PE vectors 3 to 30 contain patterns similar to those of vectors 1–2, but different phases, scales and three-dimensional

extent. This group of eigenvectors is associated with the Ionian shelfbreak/slope processes and is weakly coupled to the rest of the domain.

Fig. 10 shows the group of vectors 31 to 34. They are the first vectors which have a strong distinct signature associated with the ABV and MCC, around the basin between Pantelleria and Malta. The horizontal maps for ψ, T, S and $\hat{u}$ are shown. Singular vectors (30) and (31) are close to quadrature of phase in the horizontal. The vector (33) is close to the 90° horizontal rotation of vectors (30) and (31), with lobes related to the bottom topography (Fig. 2). The wavelength is again of order 100–140 km. For all four vectors, T and S are of opposite spatial phase in the surface, with ψ in phase with T. In difference with Fig. 9, the amplitudes of the normalized barotropic transport anomalies and corresponding external velocities (definition in Section 2.2) are about half of those of the normalized surface internal velocities and tracers, which are similar. From this group of four vectors, the result is that the dominant variability of the ABV and MCC during the period considered is mainly internal and baroclinic.

Fig. 11 is a selection of vectors which dominant signature represents patterns coupling the Ionian slope region with the basin between Pantelleria and Malta. Surface maps for T, S, $\hat{u}$ and ψ are again shown. The T maxima are at MAW depths (0–150 m) while the S maxima are at lower MLIW depths (100–400 m in this region). For all four vectors, the normalized fields of T, S, $\hat{u}$ and $\hat{v}$ (not shown) have similar amplitudes. The dominant amplitudes of the ψ anomalies and corresponding external flow are at least twice as small, excepted for the vector (44). Hence, for the vectors (36, 40, 45), as for these of Fig. 10, the velocity signatures are mainly internal. Each vector of Fig. 11 is now described successively. The T, S anomalies of vector (36) have opposite signs, adding effects on the density anomaly and thus leading to important internal velocity variability. The vector (36) accounts for internal mesoscale patterns along the Ionian slope coupled with the dominant ABV and MCC baroclinic variability patterns. The features of vector (40) are closer to the coast of Sicily, with a distinct three-lobe structure around the MCC location and again, T, S in opposition. The vector (40) is a mesoscale pattern coupling the ABV with the MCC and the western side of the IBV. Over the Ionian slope, the vector (44) shows a surface subbasin-scale tracer structure (350 to 450 km wavelength), with a strong external anomaly. The non-dimensional surface internal velocity anomaly is there twice as small as the external one (Section 2.2). The surface T, S anomalies are in phase but the T amplitude in the surface layer is three times larger than of S (S dominates at MLIW depths). Over the basin between Pantelleria and Malta, the tracer fields have opposite signs and the internal velocity anomaly, close to thermal-wind balance, dominates the external component. The vector (44) thus accounts for a coupling between mesoscale internal ABV/MCC processes and subbasin-scale external wave patterns along the Ionian slope. The vector (45) has again a subbasin-scale T, S structure over the Ionian slope (350 to 450 km wavelength). As for vector (44), in this region, the T, S surface patterns have the same sign, with the surface amplitude of T three times larger than that of S. The external pattern amplitude is there about twice that of the internal one. However, in contrast with vector (44), the signature over the Pantelleria and Malta basin dominates. Its tracer component is of large-scales, with multiple centers and the T, S maps in opposition. The internal velocity anomaly amplitude is there only almost twice that of the external (Section 2.2). The vector (45)

hence represents a coupling between mesoscale internal to large-scale external processes over the ABV/MCC with subbasin-scale external patterns above the Ionian slope. Of course, the coupled patterns shown on Fig. 11 are not imperatively physically feasible at all times. The covariance loses the sign of perturbations and the SVD imposes orthogonality constraints. Even though there is significant energy within the vectors shown, in real ocean perturbations, the couplings could cancel out at a given time by vector combinations. Other decompositions are then needed for further analysis.

To conclude, the present decomposition scheme (Section A.1) is valuable for estimating and studying the physical content of the initial variability/error covariance conditions. The results are in strong relation with the processes accounting for the main dynamical variations occurring in the Strait of Sicily during August-September 1996. Several phenomena are explained, in accord with the full PE model, horizontal mesoscale correlations and vertical EOFs of the data residuals. To agree with the data misfits around Sept. 15, the error standard deviations are estimated to be a quarter of these of the variability ($\gamma = 0.25$ in Section A.1, Eq. (A15)). For the tracers, the initial errors are horizontally uniform in the domain of interest: in the surface, the T (S) error standard deviation is 0.45°C (0.055 PSU). The corresponding initial velocity errors, obtained by PE adjustments, are largest in the Ionian slope region where the maximum gradient of the ψ error standard deviation is 1 Sv, across-slope, and the maximum surface, $\hat{u}$, $\hat{u}$ error standard deviations are 12 cm^{-1}.

3.2. Estimation with predictions of the fields and dominant error covariances

The initial field (Fig. 5) and ES (Figs. 9–11) conditions are now available. The estimation and study for the subsequent ten days can be started. Section 3.2.1 describes the results of the Sept. 15–18 forecast of the fields and ES, and of the assimilation on Sep. 18. After this, the fields and dominant error covariances are forecast to Sept. 22. The data for that day are assimilated, and new field and error forecasts issued for Sept. 24. Section 3.2.2 presents selected results from this period. All along, the estimated fields are evaluated by intercomparisons with the OI fields, clear SST images and in situ data.

3.2.1. September 15–18, 1996

3.2.1.1. Field forecast and analysis. Fig. 12 shows the surface T forecast for Sept. 18 (Panel a), the satellite SST analysis at 12:10 GMT on Sept. 17 (Panel b), and the data-forecast melded estimates of the OI scheme (Panel c) and present scheme (Panel d), both for Sept. 18. The forecast is in accord with the SST analysis for the overall shapes of the AIS front and of the main features identified in Section 3.1 (i.e., the ABV, MCC, IBV and SMV). However, at most depths, the root mean square (RMS) errors of the forecast at data-points are above the computed RMS errors of the data (Section 2.4.1). The assimilations (Panels c–d) improve this forecast. At each level, the RMS of the data residuals of the OI and present analyses are within the computed data error: Panels (c–d) are valid estimates. Nonetheless, the two assimilation schemes extrapolate the a priori data residuals differently. As shown by the northwestward velocity vectors along the

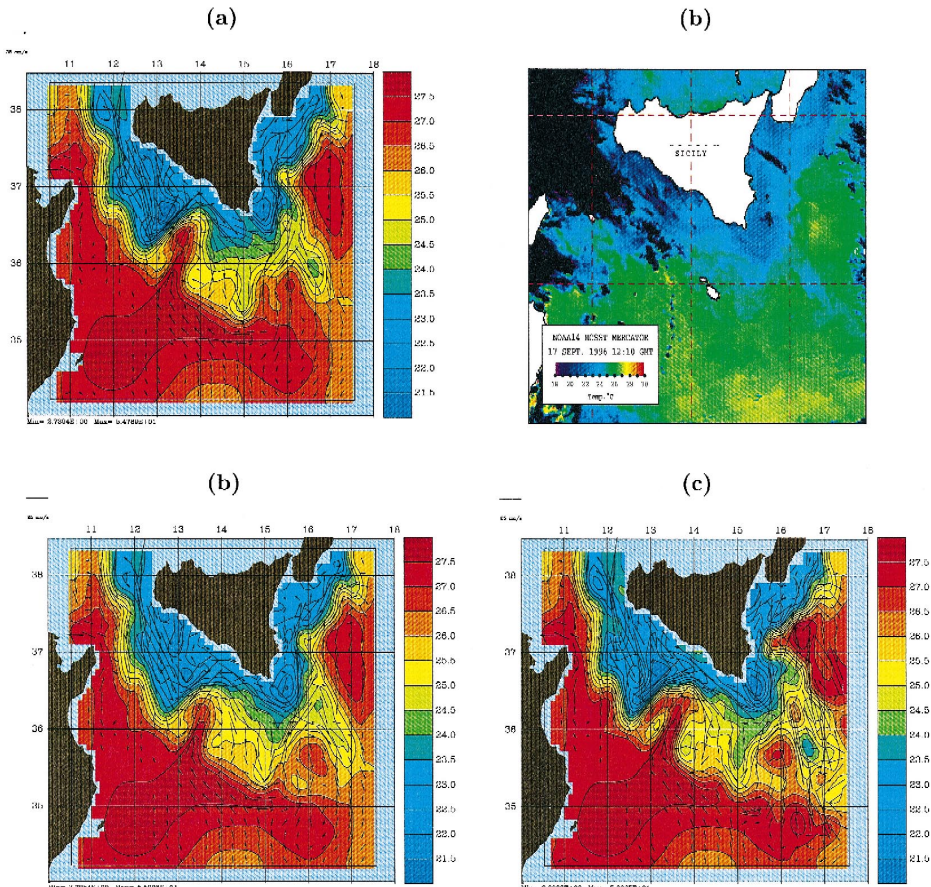

Fig. 12. Panel (a) shows the 3 day surface temperature forecast for Sep. 18, 0:00 GMT, overlaid with surface velocity vectors (scale arrow is 0.25 m/s). It is the forecast for both the OI and ESSE schemes. Panel (b) is the satellite SST distribution for Sept. 17, 12:10 GMT. Clouded regions are black (e.g., west side of the Strait). The picture was downloaded from the real-time unclassified RR96 World Wide Web server of the SACLANTCEN. Panel (c) shows the surface temperature map estimate after OI assimilation of the temperature vs. depth probes (and estimated salinities) collected on Sept. 18 (Fig. 4b). Panel (d) is as (c) but after ESSE assimilation.

southern coast of Sicily (Panel d), the present analysis immediately estimates a closed ABV while the OI (Panel c) loses the vortex structure. Similar statements are true for the SMV, south of the Stait of Messina. In the active ABV and IBV regions, the present temperature front defining the AIS free jet (Panel d) is tighter than the OI one (Panel c). In addition, comparing Panels (c–d) with the SST (Panel b), the present analysis appears closer to that of the SST. The contour and shape of the estimated IBV (Panel d) agrees with the corresponding SST feature. The OI somewhat misses the quasi-enclosed structure of the vortex by warmer water. The present estimates of the southward MAW filaments and eddy field south of the IBV are also better than their OI version. For instance, the OI has smoothed the forecast of a cold eddy pinching off the eastern side of

the IBV (Panel a) into a weak but wide filament (Panel c), while the present analysis has corrected its position (Panel d) and its temperature to ~23.5–24°C, as given by the satellite image. An issue here is that the OI imposes uniform scaling parameters, independently of the local dynamics. One may argue that the dynamical evolution subsequent to the OI assimilation could ''repair'' the OI fields. However, this adjustment is carried out at dynamical time-scales, which may be too slow. The main methodological result of the above intercomparisons is that the present analysis improves the OI one and compares well with SST nowcast.

3.2.1.2. Nonlinear forecast of the dominant error covariances. Fig. 13 deals with the convergence of the forecast of the dominant error covariance matrix for Sept. 18. Panel (a) shows the history of the similarity coefficient ρ (Section A.4, Eq. (A28)) which

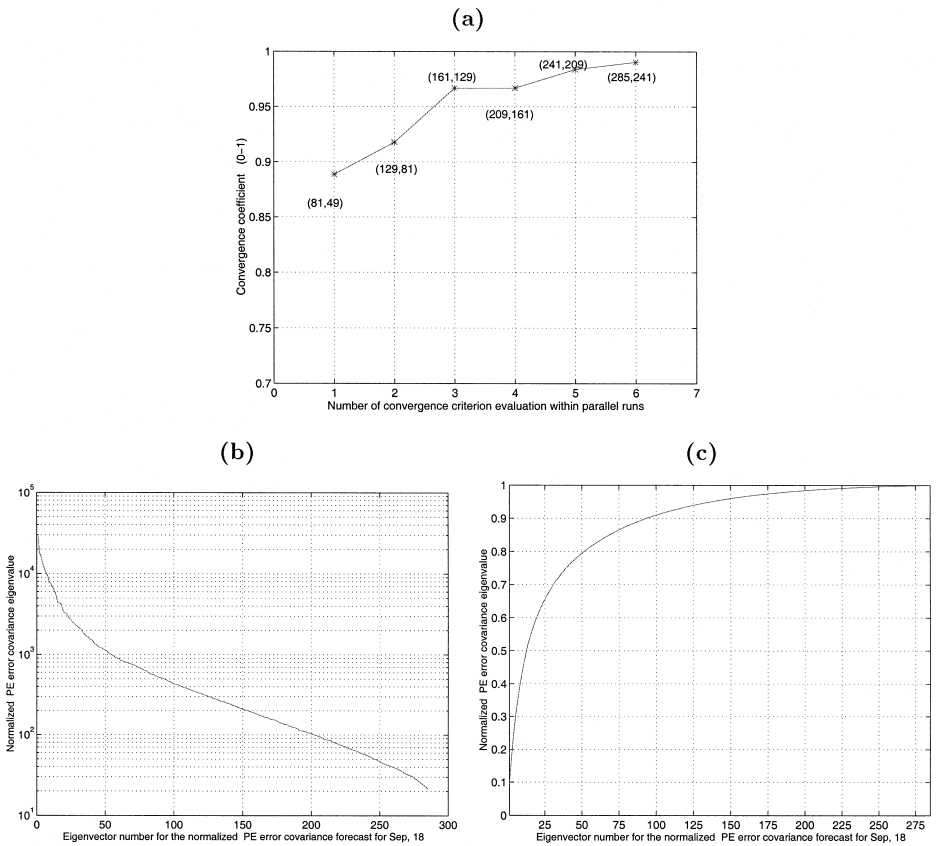

Fig. 13. Panel (a) shows the values of the similarity coefficient ρ of the ES forecast for Sept. 18. With the ensemble sizes 285 (current) and 241 (previous), ρ was 99.05%, higher than the 99% limit chosen. Parallel iterations were thus stopped. Panel (b) is the eigenvalue spectrum of the normalized ES covariance forecast for Sept. 18. Panel (c) is the cumulative (0–1) spectrum associated with (b). Utilizing 50 error eigenvectors already accounts for 80% of the variance explained by the 285 vectors; using 100 vectors accounts for 90% of that variance.

assesses the added value of new parallel batches of perturbed forecasts for Sept. 18. The chosen criterion limit of $\rho \geq 99\%$ was attained after 285 forecasts. The spectrum and cumulative spectrum of the resulting error covariance eigenvalues are described on Panels (b) and (c), respectively. An important result for the present approach is that the dominant (about first 50) eigenvalues decay faster than an exponential.

Fig. 14 illustrates the four dominant error vector forecasts for Sept. 18. They explain 25% of the error variance (Fig. 13) of the field forecast (Fig. 12a). Since model errors are assumed null, these vectors only contain nonlinearly evolved predictability uncertainties, of initial conditions illustrated by Figs. 9–11. The first vector is associated with

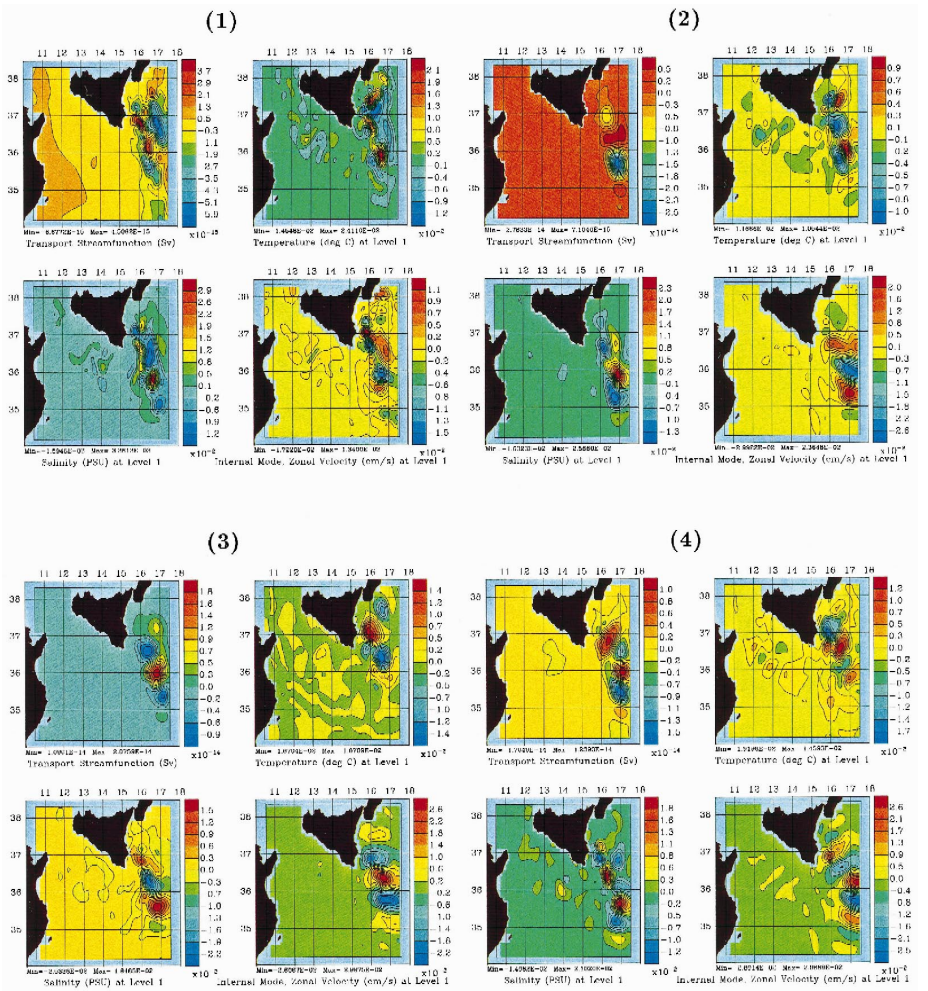

Fig. 14. Multivariate four dominant eigenvectors of the normalized, dominant error covariance forecast for Sept. 18. The Panel numbers indicate the vector numbers. The non-dimensional surface fields shown are as indicated below each plot.

mesoscale to subbasin-scale anomalies, most of which account for tracer filaments along the Ionian slope, with adjusted transport and internal velocity. These elongated T and S anomalies are close to being in phase, compensating each other in density. They could correspond to barotropically induced bifurcations of the surface AIS. Interestingly, the T and S anomalies of Panel (1) also have their largest amplitudes along the strongest portions of the temperature and salinity fronts of the Ionian slope, respectively (Fig. 5). The AIS temperature front dominates along the eastern coast of Sicily, north of 36°N to 38°N, down to about 150 m depth. In the surface, the Ionian salinity front dominates south of 36.75°N to 34.5°N, almost in parallel to 16.5°E, down to about 100 m (from around 100 m to about 220 m, the zonal horizontal gradient of this salinity front reverses in accord with the MLIW rising on the shelf). Hence, the first vector corresponds to possible bifurcations of the AIS and to fluctuations in the positions of the ''Ionian slope fronts''. Note that it is the study of such forecast eigenvectors that clearly revealed the different latitudinal locations of these temperature and salinity slope fronts. The second, third and fourth vectors (Panels 2–4) contain baroclinic/barotropic topographic Rossby wave patterns along the Ionian slope that are roughly similar to those of the initial ES conditions (Fig. 9). The T and S surface anomalies are larger than initially and are mainly restricted to their respective fronts. The external component is relatively strong: the surface internal flow anomalies are about twice as large as the external ones (definition in Section 2.2). These forecast vectors (2–4) are dynamically adjusted to the PE field conditions of Sept. 18, with nonhomogeneous, anisotropic patterns and scales. Higher eigenvectors show error patterns in the Ionian slope, ABV, MCC, IBV and SMV regions. Some are intrinsic to a region, others show coupled patterns, with local wavelengths ranging from 20 to 500 km. Scales are generally larger at mid-depths than in the surface and bottom layers. For most eigenvectors, the scales are not as separated as in the initial ES conditions (Figs. 9–11) and the energy ordering does not strictly follow scales. There are multiple scales in three-dimensions on most vectors, with complex, nonhomogeneous patterns, different from regions to regions.

Fig. 15 shows the RMS predictability error forecast corresponding to the forecast of Fig. 12a. Panel (a) shows the ψ and surface T, S and $\hat{u}$ errors; Panel (b) shows the level-10 T, S $\hat{u}$ and $\hat{v}$ errors. Initially, the tracer errors were horizontally uniform in the domain of interest and the velocity errors corresponded to PE adjusted responses (Section 3.1). During Sept. 15–18, this has evolved. In the surface (Panel a), the most dynamically uncertain features are the Ionian slope fronts (ψ, T, S, $\hat{u}$) and the meanders of the AIS along the ABV and MCC (T, S and $\hat{u}$). The T and S error fields confirm the different locations of the temperature and salinity slope fronts. The ψ error field supports the Ionian slope as the region of largest variations of external variability. On level-10 (Panel b), the temperature is most uncertain within the IBV and associated filaments ($\sim$ 20–30 m depths), while the salinity is most uncertain along the Ionian slope ($\sim$ 70–150 m depths) and along a MLIW path to the Western Mediterranean ($\sim$ 40–60 m depths). An implication of these results is that, for several locations and features, the dominant variations of variability during Sept. 15–18 correspond to specific state variables, indicating the need for particular data.

The nonlinear dynamical evolution of the error covariance function is portrayed by Figs. 16 and 17. Fig. 16 recalls the initial shapes (Section 3.1). Precisely, the variability

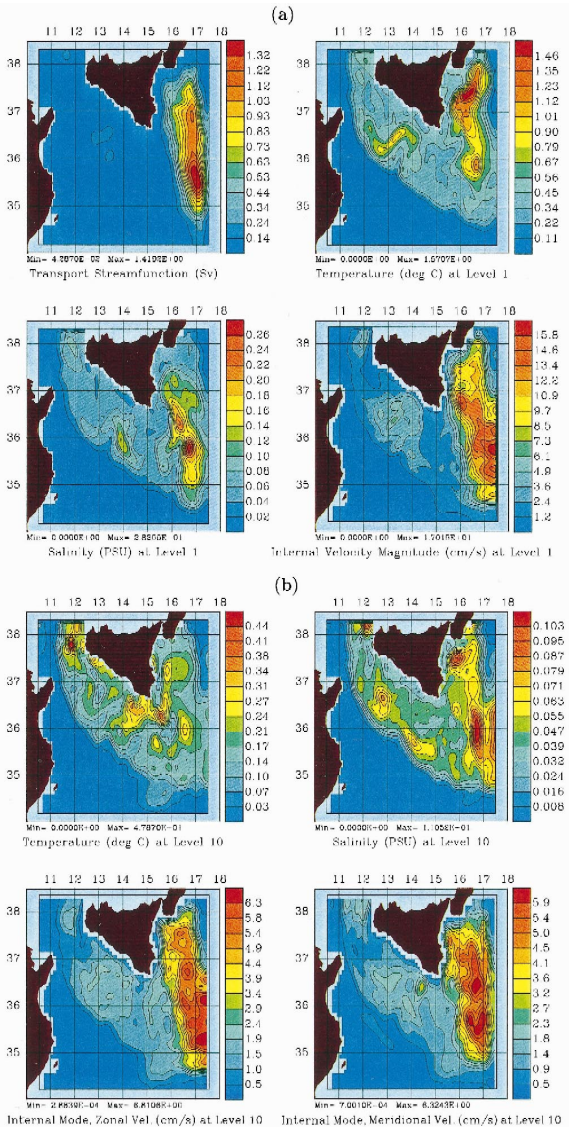

Fig. 15. Root-mean-square error forecast for the PE field forecast of Sep. 18 (Fig. 12a). Panel (a) shows surface errors, Panel (b) level 10 errors (from 30 m over the Strait to 140 m off the Ionian slope).

covariance between the surface temperature at (36.53°N, 13.40°E) and the other state variables on Sept. 15 is shown. A row of the covariance matrix is thus considered. Looking at the tracer covariances, even though only the dominant 289 PE singular vectors are used, the initial horizontal ''Mexican hat'' and vertical EOF structures (Section 3.1.1) are well represented. The corresponding velocity cross-covariances are shown by the ψ, $\hat{u}$ and $\hat{v}$ fields. Measuring T at (36.53°N, 13.40°E) on Sept. 15 would

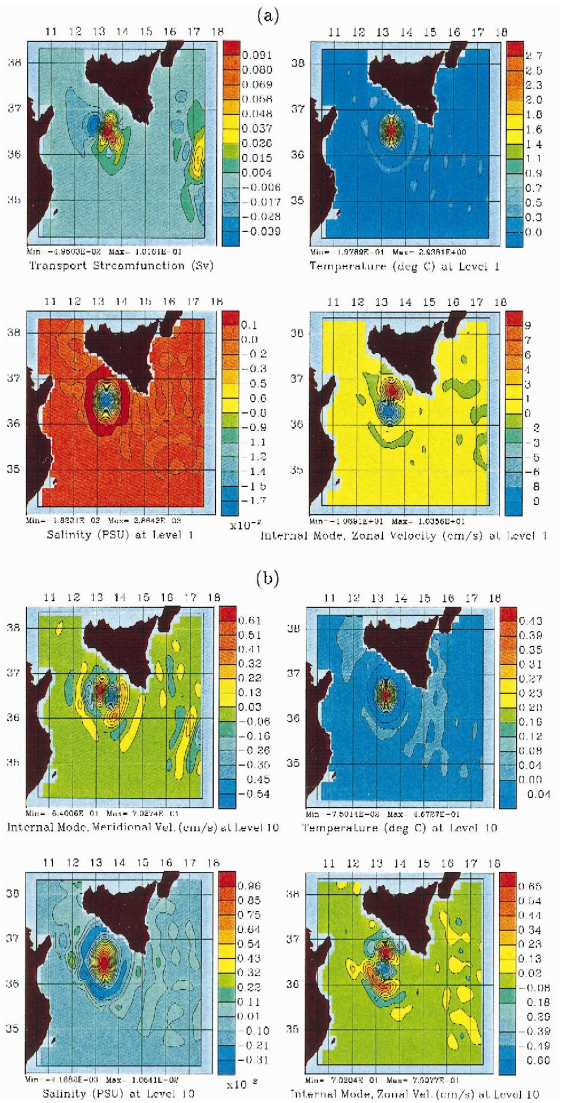

Fig. 16. *Initial* PE variability covariance estimate between the surface temperature at (36.53°N, 13.40°E) and the other state variables. The first and tenth level components of a row of the covariance **P** on Sept. 15 (size 299,052×299,052) are shown. Panel (a) shows the surface values, Panel (b) the values for level 10.

influence S, ψ, $\hat{u}$ and $\hat{v}$ according to the structures of Fig. 16. Such structures would be on the LHS of the gain $\mathbf{K}^p$ (Section A.2), extrapolating the data residuals onto the PE state vector.

Fig. 17 is as Fig. 16, but for the Sept. 18 forecast. It exemplifies the covariances that extrapolated the Sept. 18 data residuals in the analysis of Fig. 12d. The nonlinear variations of variability have modified the initial structures (Fig. 16). The surface scales

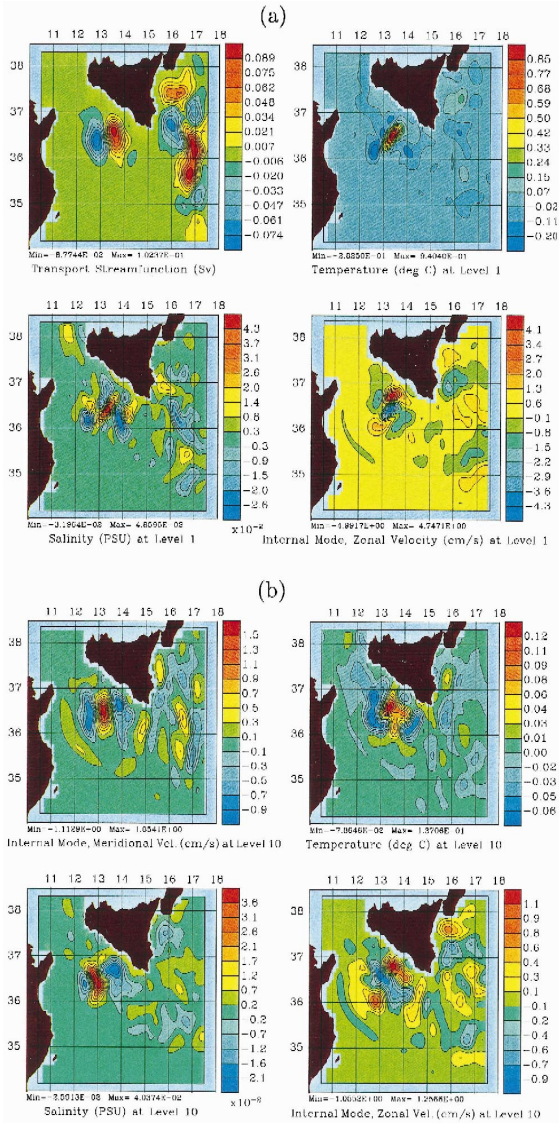

Fig. 17. Same as Fig. 16, but for the dominant error covariance *forecast* for Sept. 18.

(Panel a) are now smaller than these at the bottom of the thermocline (Panel b). The T auto-covariance (top right of Panels a–b) is elongated along (~ 80 km), but much shorter across (~ 15 km), the local energetic MCC meander (Fig. 12). The negative part of the initial ''Mexican hat'' pattern is modified in accord with the AIS advection path (top right of Panel a). The top right of Panel (b) is the covariance between the surface T at (36.53°N, 13.40°E) and T at the bottom of the MAW layer (level 10). It has a positive center, extending in three lobes and covering a wider region than the corresponding

surface feature (top right of Panel a). The T–S cross-covariance has equally dynamically evolved towards more complex shapes (bottom left of Panels a-b), and has now weak connections with Ionian slope processes. Comparing the T-$\hat{u}$ (bottom right of Panels a–b) and T–$\hat{v}$ (top left of Panel b) with their initial values (Fig. 16), in the surface, they are tighter across and more elongated along the AIS meander (Fig. 12), and, on level 10, they are wider and longer. Finally, the T-ψ cross-covariance (top left of Panel a) has larger and rounder scales than initially, with a signature both within the Strait basin and Ionian slope region. Other such fields (Lermusiaux, 1997) show depth, region and process dependent horizontal scales. Near coastlines, the tracer auto-covariances are often close to coast-truncated ''Mexican hats''. Along the Ionian slope, the momentum (cross)-covariances usually consist of decaying wave patterns. Similar statements can be made for the vertical scales.

In conclusion, the error covariance has evolved according to the dominant nonlinear variations of the variability, with scales and processes a function of the region and depth considered. It is challenging to incorporate such complexities in the OI scheme. Setting the assimilation aside, ESSE can track and organize the nonlinearly evolving predictability/variations of variability subspaces. Further studies of such subspaces and dominant covariances, with perhaps subsequent analysis using mathematical tools tailored to the phenomena of interest (e.g., energy and vorticity analysis via ESSE), should be very helpful in understanding complex multivariate geophysical systems.

3.2.1.3. Dominant error covariances after assimilation and error learning. The a posteriori 3D multivariate RMS error fields corresponding to the analysis plotted on Fig. 12d have been exemplified by the real-time map of Fig. 1c. As one would expect from uniform mesoscale error weights, the error is reduced around the location of the data. However, the peculiarities of the dynamics affect this simple result (Lermusiaux, 1997). Briefly, the error is for example reduced along the advection path of the meandering AIS, all across the Channel. East of the missing data region at (35.6°N, 16.4°E) (Fig. 4b), the error reduction has tighter zonal scales than elsewhere, in accord with the local predictability error patterns portrayed on Fig. 14 (AIS bifurcations or filaments along the slope, etc). In practice, such a posteriori error fields are useful to design future sampling strategies (Section 1). Their 3D multivariate values (not shown) indicate that to best reduce uncertainties on Sept. 18, one should investigate the MCC, SMV and deep Ionian slope regions, with both hydrographic and velocity sensors.

Fig. 18 illustrates the adaptive component of the present estimation methodology: the dominant error covariance matrix is learning (e.g., Brockett, 1990) from the possibly significant data residuals. The procedure is detailed in Section A.3. On Sept. 18, the a posteriori residuals are first objectively analyzed. Their surface values are shown on Panels a–b. The amplitudes of the gridded T residuals are below the T measurement error, but those of the S residuals are at some locations larger than the S measurement error. This could be due to the approximate salinity data estimate (Section 2.3) or to the neglected model errors. The significant residuals are then combined with the a posteriori error subspace, leading to an ''adapted'' error subspace estimate (Section A.3, Eqs. (A22) and (A23)). Presently, their effect distinctly shows up within the adapted error eigenvectors 80 to 90; the surface salinity of the adapted vector 81 is given on Panel (c)

for example (compare with Panel b). The eigenvalue and cumulative spectra of the corresponding (after the assimilation and error learning on Sept. 18) normalized error

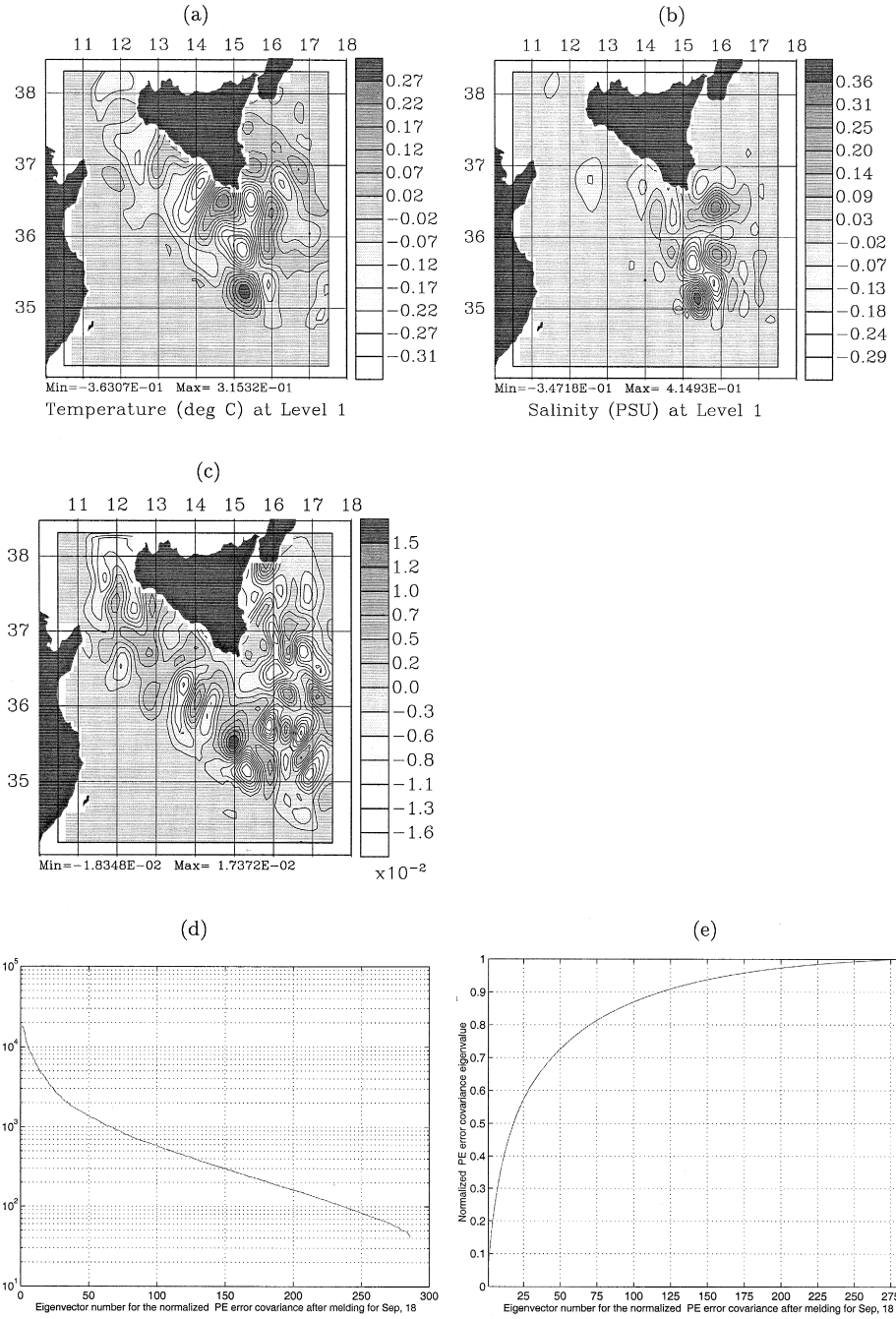

covariance matrix are plotted on Panels (d) and (e), respectively. In comparison to the a priori or forecast quantities (Fig. 13b–c), the assimilation has logically flatten the error spectrum.

Fig. 19 shows the surface values of the four dominant a posteriori and adapted error eigenvectors. The first three vectors mainly explain temperature driven wave-patterns and AIS meanders along the eastern coast of Sicily (data were not assimilated in this region). The fourth vector is a salinity related pattern on the southern part of the Ionian slope, with a temperature signature at the northeastern open boundary. These dominant vectors differ from the forecast ones (Fig. 14). The assimilation has decreased the error amplitude and reorganized the error structure, in agreement with the data innovations.

3.2.2. September 18–24, 1996

Selected results of the estimation and study subsequent to the assimilation on Sept. 18 are presented. Some aspects of the adaptive evolution of the error covariances are summarized. The features and variabilities of the physical fields are discussed and their estimation is evaluated by intercomparisons with the OI fields, SST images and in situ data.

The assimilations on Sept. 18 and Sept. 22 (Fig. 4b–c) introduce the non-uniform properties of the data (specific variables, resolution in space and time, localized sampling) into the error statistics. The adaptive evolution of the error covariance is now influenced by the statistics of both the observations and dynamics. For example, the similarity coefficient ρ (Section A.4) between the ES forecasts for Sept. 18 and Sept. 22 is,

$$\rho_{18-22} = \frac{\sum_{i=1}^{285} \sigma_i \left(\overline{\Pi_{18}^{2}}(-)\, E_{18}^{T}(-)\, E_{22}(-)\, \overline{\Pi_{22}^{2}}(-) \right)}{\sum_{i=1}^{292} \sigma_i(\Pi_{22})} = 58\%. \qquad (2)$$

Even though the two ES forecasts have similar sizes (285 and 292), their amplitude and structure are only 58% alike. Similar comments apply to the Sept. 22 and Sept. 24 ES forecasts. For each of the Sept. 18–22 and Sept. 22–24 periods, the terminal prediction of the dominant error variance (not shown) also indicates that the error growth is tempered downstream of the sampling locations. The scales and patterns of the corresponding error eigenvector forecasts confirm that these data influences are in accord with the features identified in Sections 3.1 and 3.2.1. For the Sept. 18–22 error forecast, the features involved are the ABV, MCC, IBV and Ionian slope fronts. For the

Fig. 18. Adaptive learning of dominant errors. Panels (a–b) show the surface *T*, *S* gridded a posteriori data residuals as estimated by ESSE objective analysis on Sept. 18. Panel (c) is the surface *S* of error vector number 81 after adaptation. This vector explains parts of the residual shown by (b). Panel (d) is the eigenvalue spectrum of the normalized ES covariance after adaptation. Panel (e) is the cumulative (0–1) spectrum associated with (d). Using 50 vectors explains 73% of the variance explained by the 286 vectors; 100 vectors explain 87% of that variance. Comparing with Fig. 13, the assimilation flattens the error spectrum.

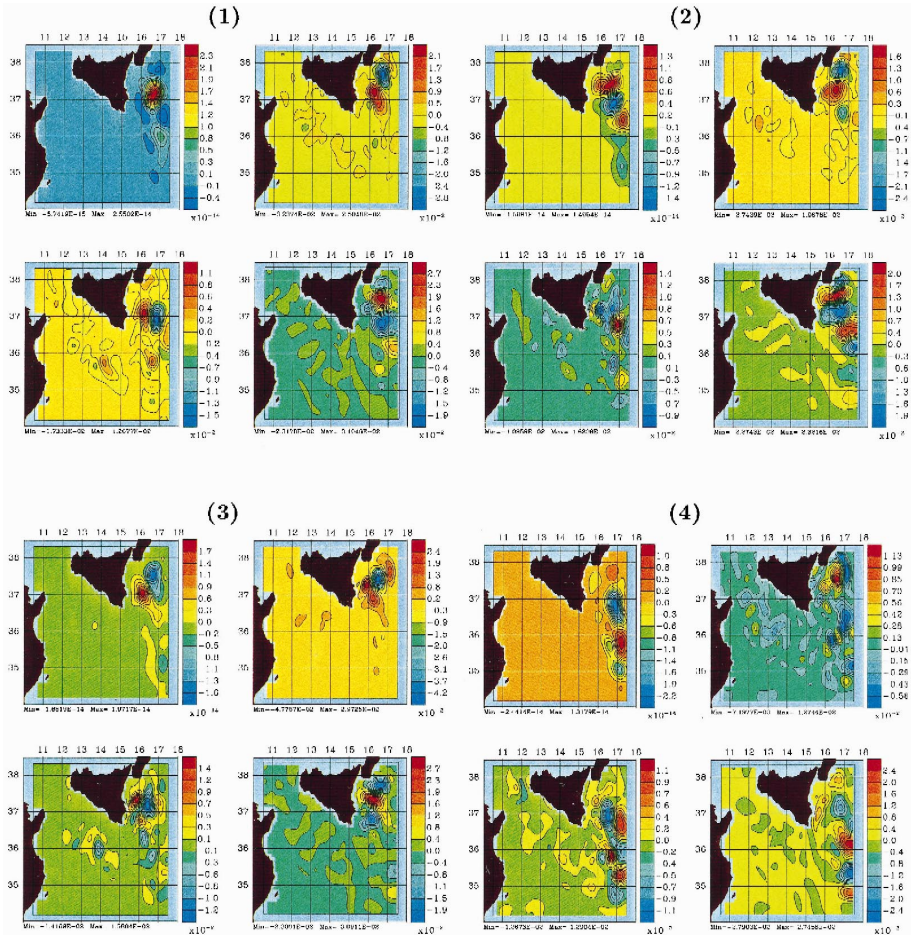

Fig. 19. Multivariate four dominant eigenvectors of the normalized, dominant error covariance after ESSE assimilation and error subspace learning on Sept. 18. The Panel numbers indicate the vector numbers. The non-dimensional fields are from left to right, top to bottom: the barotropic transport and the surface temperature, salinity and zonal internal velocity.

Sept. 22–24 error forecast, the features involved are the IBV and a portion of the Ionian slope fronts. In general, the real-time use of such predicted results should be valuable for optimizing the choice of sensors and sampling patterns. As exemplified by Eq. (2), the relatively low similarity between ES forecasts also indicates that a sub-optimal approach where (parts of) the ES are kept stationary for some time requires careful sensitivity studies, even for an interval within the predictability limit of the scales considered. Such ideas are further discussed in (Lermusiaux, 1997).

Fig. 20 shows surface temperature estimates for Sept. 23, which is after the two assimilations. The present forecast is plotted on Panel (a) and the OI one on Panel (b). Panel (c) is the satellite SST analysis at 12:45 GMT on Sept. 23. As argued later, the

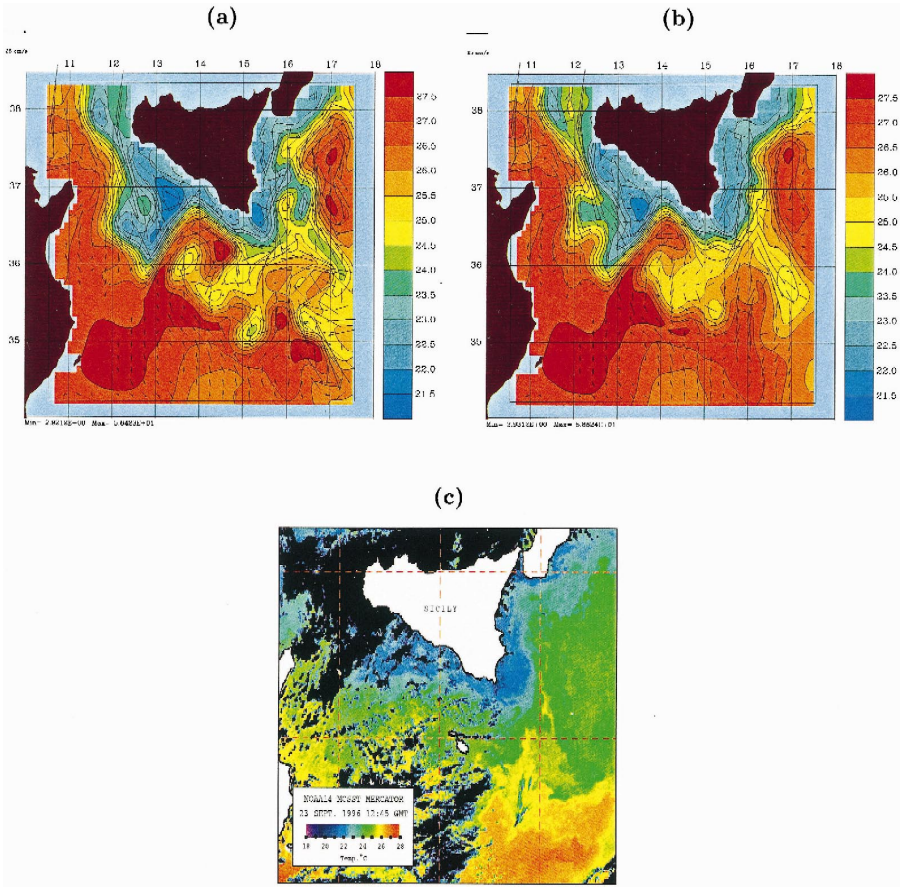

Fig. 20. Panel (a) shows the 8-day ESSE surface T forecast for Sept. 23 (a 1-day forecast from the ESSE fields of Sept. 22), overlaid with surface velocity vectors (scale arrow is 0.25 m/s). Panel (b) is as (a) but for the OI (a 1-day forecast from the OI fields of Sept. 22). For each, an assimilation occurred on Sept. 18 and 22. Panel (c) is the satellite SST distribution for Sept. 23, 12:45 GMT. The scale differs from that of Fig. 12b. Clouded regions are black. The picture was downloaded from the real-time unclassified RR96 World Wide Web server of the SACLANTCEN.

present estimation gives the overall best fields. The evolution of the features whose variations dominate the variability during RR96 (as identified in Sections 3.1 and 3.2.1) is thus best illustrated by comparing Fig. 20a with Fig. 12d. Considering these features from west to east, the ABV has deepened to the southeast, with parts of the AIS flow pinching off a warm mesoscale eddy around (36.7°N, 12.8°E). The MCC has strengthened and moved northeastward. It has advected warm Tunisian shelf waters along its path and induced a recirculation of MAW origins to the southwest, which is now leading to a cold mesoscale eddy around (36°N, 13.6°E). The IBV has reduced its strength and horizontal extent, somewhat moving to the eastern coast of Sicily, north of Syracuse. The T and S fronts of the Ionian slope have been associated with a substantial

mesoscale to subbasin-scale variability. Their evolutions and several of the MAW mesoscale eddies formed east of 13E and south of the AIS are discussed next, as part of the field evaluation.

The present estimates (Fig. 20a) are first evaluated by intercomparisons with the OI ones (Fig. 20b). After the assimilations, the two melded fields differ significantly even though they each have RMS data misfits within the estimated measurement error

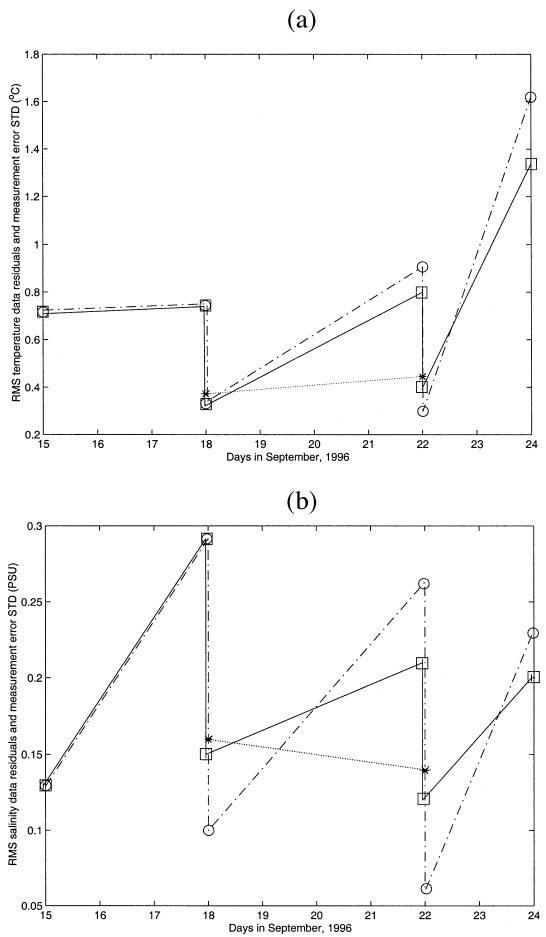

Fig. 21. Panel (a) shows the surface averaged (top 5 levels) root mean square (RMS) a priori and a posteriori residuals with respect to the temperature probes collected on Sept. 18, 22 and 24 (Fig. 4b–d). Data are only assimilated on Sept. 18 and 22. On Sept. 15, the RMS was taken with respect to the probes of Sept. 18 for skill evaluation. The curve in red is the RMS for the OI, the blue curve is for the ESSE. Using this RMS measure, the present temperature forecast is 14% better than the OI one for Sept. 22 and 21% better for Sept. 24. The green curve is the surface averaged (top 5 levels) of the measurement model RMS error used in ESSE. Panel (b) is as (a) but for salinity. The present salinity forecast is 25% better than the OI one for Sept. 22 and 16% better for Sept. 24.

bounds. This is due to the different error weights, which during RR96 often yield to OI fields smoother than the ESSE ones. Outside of the assimilated data regions (Fig. 4b–c), the data corrections are advected downstream of the dominant features, e.g., along the AIS meanders and Ionian slope fronts. The Ionian slope region is in fact where the two fields differ the most. Since there is no in situ verification data at these locations, the SST image on Sept. 23 (Fig. 20c) is used for qualitative evaluations. Describing the estimates southward along the Ionian slope, the present estimate (Fig. 20a) is closer to the SST image than the OI one for each of the following features: the southward AIS meander off the coast of Calabria; the U-shaped pattern of warm Ionian water towards the eastern Sicilian coast; the 16E intrusion of Ionian water off Syracuse (36°N to 37°N); the adjacent MAW extrusion along the slope from 37°N to 35.3°N, suggesting an AIS bifurcation; the 25.5–26C, 70 km radius anticyclonic eddy centered around (35.7°N, 16.1°E); the two cold, 20 km radius mesoscale eddies at (35.2°N, 15.2°E) and (35.3°N, 16.5°E); and finally the IBV and its southwestward tongue entrained in the MCC.

The quantitative evaluation of the present field estimates is carried out using the in situ data. On average, within the new data regions (Fig. 4c–d), the level by level RMS of the forecast-data misfits at data-points give an ESSE forecast 10 to 20% better than the OI one, depending on the depth considered. Fig. 21 summarizes these results, plotting the Sept. 15–24 evolution of the surface-averaged (top 5 levels) data misfits at data-points. The OI is in red, the adaptive ESSE in blue. Both curves are the same up to Sept. 18. The measurement RMS error given by ESSE (Section 2.4.1) is shown in green, again on average for the top 5 levels: it increases for T, but decrease for S, in accord with the average variability tendencies (Panels a–b). All melded estimates have a RMS error below that measurement RMS error. Nonetheless, the present surface forecasts are on average about 20% better than the OI ones, even though the melded OI fields have smaller data misfits. For example, the Sept. 24 ESSE data-forecast misfit at data-points is for T, 21% better, and for S, 16% better, than the OI one. This is encouraging since the sampling of Sept. 24 (Fig. 4d) revisits the IBV domain already measured on Sept. 22 (Fig. 4c). The large temperature RMS error increase for both schemes on Sept. 24 is due to their slightly off-positioned forecasts of the IBV front. Considering salinities (Panel b), even though the OI/ESSE salinity RMS misfits decrease steadily, the salinity forecast errors grow rapidly. This may indicate that the estimation of the AXBT salinities (Section 2.3) could be improved. Finally, looking at the SST on Fig. 20c, the evaluation based on localized data (Fig. 4b–d) may underestimate the performance. The overall improvements could be higher than 20%.

4. Summary and conclusions

In the foregoing paper, the ESSE approach was applied in real-time for a period of ten days during the NATO operation RR96, considering mesoscale variability in the Strait of Sicily. Combining the intensive RR96 data survey with the primitive equation model of HOPS (e.g., Robinson, 1996), the estimation and study of the physical fields and their dominant variability and error covariances were carried out. The four-dimen-

sional adaptive estimation methodology was illustrated and evaluated. The corresponding technological achievements and scientific progress were presented and studied.

Technology-wise, this experiment and similar studies in several regions of the world's ocean (Robinson et al., 1998c) demonstrate that the ESSE system is a portable and comprehensive nonlinear assimilation scheme for realistic mesoscale to large-scale ocean studies, capable of providing real-time estimates of ocean fields and associated error and variability covariances. Presently, its main components involve the PE model of HOPS, the initialization and parallel ensemble forecast of the error subspace, the sequential assimilation, the dynamic measurement model, the adaptive learning of the dominant errors and the verification modules. The system confirmed that the dominant error eigenvalues have a decay faster than exponential and the ES convergence criterion employed showed that an ES dimension of order 300 sufficed for the considered RR96 experiment. The present nonlinear scheme is thus here about $299{,}052/300 \sim 10^3$ times cheaper than classic, full-covariance and linear methods (e.g., Robinson et al., 1998a). For identical computer power, such methods would need more than 8 years for the ten days of estimation. Yet, sensitivity studies on the size of the ES and improvements of the parallel forecast networking suggest that the present elapsed-time could be further reduced by half. Considering sub-optimal schemes for rapid operations, one could also keep the ES constant for some time, hence using a piece-wise stationary ES. Other simplifications only perturb regions in which future data are known to be gathered or use simple models for the error eigenvalue growth, keeping the eigenvectors fixed. Such considerations are first steps towards rapid, nested and multiscale assimilation systems in multiple regions.

The estimated fields were evaluated by intercomparisons with OI fields, clear SST images and available in situ data. Qualitative comparisons with the OI fields clearly showed the advantage of the present error weights (covariances) which are multivariate, multiscale, anisotropic and commonly non-uniform in space and time, in accord with the evolving data and dynamics. Quantitatively, the forecast-data misfits at the in situ observation points around the Ionian Shelf Break Vortex region implied that the present forecasts were, on average, 20% better than the OI ones. Qualitative comparisons with SST images over the complete model domain suggested much higher improvement factors. Note that the OI is nonetheless a robust scheme and a useful assimilation quality benchmark. It is cheaper than the present scheme by a factor approximately equal to the size of the ES divided by the number of CPUs used in parallel. In this study, 12 to 16 Sun Sparc 20 CPUs were employed, depending on availability. Improving the OI scheme from analyses of the present error weights is thus useful, especially for large-domain, rapid assimilations. In general, ESSE simulations can be used for comparison and refinement of cheaper assimilation techniques.

Several scientific results were also obtained. The dominant decomposition of the initial PE variability covariance matrix has determined several of the features associated with the dominant variability in the Strait of Sicily during August–September 1996. Five coupled features emerged: the Adventure Bank Vortex (ABV), the Maltese Channel Crest (MCC), the Ionian Shelf Break Vortex (IBV), the intermittent Strait of Messina Vortex (SMV) and the subbasin-scale temperature and salinity fronts of the Ionian slope and their corresponding wave patterns. The first three of these features were also

subjectively identified during independent RR96 forecast evaluations and named by Robinson et al. (1998b). The sustained presence of the ABV, MCC and IBV during RR96 is likely due to the squeezing and stretching of the AIS over the Adventure Bank and Maltese plateau, to the prevailing mean westerly winds maintaining an upwelling balance on the southern coast of Sicily and to the inertia of the isopycnal domes. The intermittent SMV lacks these topographic and mean wind controls, and could be unsettled by meandering southward shelf currents (Böhm et al., 1987). From this identification, it is of interest to study the dynamical relationships and interactions between these five features and the double MAW and MLIW flow system of the Sicily Channel. A complete understanding of these relations and their variabilities at multiple time and space scales should be valuable for Mediterranean science.

A small step in this direction was provided by the present study of ten days of estimated physical fields and dominant error covariance decompositions, revealing several of the 3D-multivariate PE processes associated with the variations of the above five features. In the Ionian slope region, filaments and bifurcations of the AIS into several streams as well as meanders of the temperature and salinity slope fronts were suggested by the field evolution and confirmed by the dominant predictability eigenvectors. This dominant variability involved mesoscale to subbasin-scale baroclinic and barotropic topographic wave patterns. The tracer and internal flow anomalies were close to thermal-wind balance and mainly limited to 0–500 m. The corresponding barotropic transport anomalies were shown to have their largest amplitudes in this region and to be influenced by baroclinicity, relief, diffusion and nonlinear effects. In the ABV and MCC region, the dominant variability was of a mesoscale, internal and baroclinic nature, not far from geostrophic equilibrium. The internal flow anomalies usually dominated the external ones and were supported by temperature and salinity anomalies often adding effects in density. If couplings between the Ionian slope, IBV and ABV/MCC regions occurred, they appeared to involve subbasin-scale external processes and mesoscale, baroclinic internal processes, possibly occurring simultaneously in both regions. South of the AIS, a substantial mesoscale activity with several MAW eddies was estimated and forecast with accuracy by the present scheme. Considering water masses, the salinity variability and error patterns associated with the deep MLIW and with the Tunisian shelf and Ionian waters were found to be linked with the variations of the properties (pycnocline depth, vertical and horizontal scales, overall strength) of the surface-intensified features presently revealed. In general, the scales of the dominant predictability error covariances in the Strait were usually observed larger at mid-depths than in the surface and bottom layers. These scales and associated error patterns were often not separated, implying the possibility of coupled multiscale interactions. In fact, the dominant eigendecomposition of covariance matrices did not follow a simple scale ordering. Looking at covariance function fields, the dynamical evolution over realistic topography induced nonhomogeneous and locally anisotropic 3D maps, with complex multivariate correlations, in accord with the evolving properties of the physical fields.

In general, the above facts show how the present approach can continuously decompose, organize and track the dominant nonlinear ocean variability. It was found here, and confirmed in other ocean regions, that the three-dimensional variations of variability of a feature are often associated with *groups* of predictability eigenvectors

and eigenvalues. This is in part due to the orthogonality constraint, but is also a reflection of the coupled multiscale, multivariate and nonhomogeneous nature of the real ocean variability. Once the evolving dominant eigendecomposition has been estimated and studied as in this presentation, subsequent analyses should thus be very informative. For example, additional tools could disentangle the processes from the estimated subspaces (e.g., Fourier, wavelets, factor or cluster analysis). Another direction consists in studying the time-space evolution of diagnostic quantities, e.g., energy, vorticity or enstrophy principal components. The four-dimensional estimation and dominant decomposition of statistical properties other than the fields and covariances should also be a fruitful sign of research.

These few technological and scientific advances are linked to practical data and model feedbacks. First, the dominant error covariance eigendecomposition and error variance fields are useful to estimate data requirements for a specific experiment. From the present study, the importance of the deep MLIW variability and error patterns suggests that, for accurate three-dimensional estimations, both salinity and temperature should be measured in the Sicily Strait, at least down to about 500 m. The need of current data in the Ionian slope region was emphasized, especially for the external component (e.g., moorings, ADCPs, AUVs). For some regions, periods and features, the dominant uncertainties were also observed to be associated with specific state variables, for example: T for the IBV, S for a MLIW path or T (S) with total velocities for the temperature (salinity) Ionian slope front. In general, the error growth was logically tempered downstream of the sampling locations. It was also found that the impacts of observations were determined by the most uncertain variations of the five features identified. For example, the data impacts had tight horizontal scales across the Ionian slope, in accord with the most uncertain local fluctuations of the corresponding subbasin-scale fronts. Hence, evolving these dominant variations or predictability errors appears most valuable for adaptive sampling design. The present approach in fact allows to forecast data optimals, i.e., the most desired and least expensive future observational strategy (sensor and platform types, sampling pattern) within the available observational networks. Such a scheme, combined with practical and meteorological constraints, was used subjectively during the March 98 Rapid Response in the Gulf of Cadiz for the adaptive design of AXBT flight patterns (Robinson et al., 1998c). With the implementation of real-time optimal control and optimization algorithms, computed data optimals give the ESSE scheme the observations it needs most, hence ideally improve the ocean estimate. Secondly, the focus on the largest errors has been very helpful to refine the dynamical and measurement models employed in the real-time experiment. The open boundary conditions, coastal and bottom friction parameterizations, Shapiro filter and error models have for example been improved. Such feedbacks are important and during the more recent Rapid Response 97 in the Ionian Sea (Robinson et al., 1998c), additional model improvements were achieved.

Acknowledgements

This paper is dedicated to Professor Allan R. Robinson. When he returned from the RR96 cruise, I handed him a report on the present real-time estimation and study. A few

days later, he rushed into the graduate student's office with an ear-to-ear grin. By analyzing the at-sea field forecasts, he had also identified in real-time the ABV, IBV and MCC as features of dominant variability. He did not need the covariance eigendecompositions. For those of us who have had the chance of being at-sea and in real-time oceanography pressures, one can only be fascinated. It is a pleasure to acknowledge the continued stimulation, interest and encouragements of such a prodigious scientist of the real ocean. Several people have contributed to this work. I benefited greatly from the members of the Harvard oceanography group, past and present. In particular, I am thankful to Dr. Carlos J. Lozano for some comments. I am grateful to two anonymous referees for their helpful reviews. I thank Mr. Michael Landes and Mr. Todd Alcock for preparing some figures for this manuscript. This study was supported in part by the Office of Naval Research under grants N00014-95-1-0371 and N00014-97-1-0239 to Harvard University.

Appendix A. Error subspace statistical estimation scheme employed

The main notation used and the estimation scheme employed are summarized. The intent is simply to provide an helpful and concise overview. For more on such methodologies, we refer to Lermusiaux (1997, 1998), Lermusiaux et al. (1998), and Lermusiaux and Robinson (1998). Related ensemble techniques for nonlinear data assimilation are addressed in (Evensen, 1994; Burgers et al., 1998; Miller et al., 1998). The so-called reduced state-space Kalman filters are discussed in a geophysical context for example by Cane et al. (1996) and Cohn and Todling (1996). The aim here is to reduce the error statistics in a fashion consistent with the assimilation criterion used. The present framework is that of a continuous-discrete estimation (Jazwinski, 1970). The gridded values of the PE fields, $\hat{u}$, $\hat{v}$, T, S and ψ are combined into the state vector $\psi = (\hat{u}, \hat{v}, \mathbf{T}, \mathbf{S}, \mathbf{p})^T \in \mathbb{R}^n$. For the internal velocities $\hat{u}$, $\hat{v}$ the convention of Cox (1984) is kept; in all other cases, $(\hat{\cdot})$ is the ''estimate'' operator (Gelb, 1974). Model errors are assumed null. The dynamical evolution of the ocean state ψ is described by,

$$\mathrm{d}\psi = \mathbf{f}(\psi, t)\,\mathrm{d}t, \tag{A1}$$

where $\mathbf{f}(\cdot, t)$ is the nonlinear PE operator, including boundary conditions and forcings. Data at time t_k are stored in $\mathbf{d}_k \in \mathbb{R}^m$. The measurement model associated with Eq. (A1) is

$$\mathbf{d}_k = \mathbf{C}_k \psi_k + \mathbf{v}_k. \tag{A2}$$

The $\mathbf{v}_k \in \mathbb{R}^m$ are random processes, assumed of zero statistical mean and of covariance matrix $\mathbf{R}_k$, with $\varepsilon\{\mathbf{v}_k\, \mathbf{v}_j^T\} = 0$ for $k \neq j$. The state error covariance matrix at t_k is defined by $\mathbf{P}_k \doteq \varepsilon\{(\hat{\psi}_k - \psi_k)(\hat{\psi}_k - \psi_k)^T\} \in \mathbb{R}^{n\times n}$. The notation $\varepsilon\ \{\mathbf{g}\}$ refers to the statistical mean of a given state space functional $\mathbf{g}$. At times t_k, to refer to quantities before and after the assimilation, the adjectives a priori $(-)$ and a posteriori $(+)$ are used, as in Gelb (1974). When the index k can be omitted, the $(-)$ and $(+)$ besides singular vectors are simplified to subscripts.

Table 3
Filtering via ESSE at t_k: continuous-discrete problem statement

Dynamical model	$\mathrm{d}\psi = \mathbf{f}(\psi,t)\mathrm{d}t$, with $\hat{\psi}_0 = \Psi_0$.	(A1)
Measurement model	$\mathrm{d}_k = C_k\psi_k + \upsilon_k$.	(A2)
Error subspace	$\{\Pi_k, \mathbf{E}_k$ with $\mathbf{P}_k^p = \mathbf{E}_k\,\Pi_k\mathbf{E}_k^T$ and $\mathrm{rank}(\mathbf{E}_k) = p \mid \min_{\Pi_k,\mathbf{E}_k} tr[\mathbf{P}_k^c]\}$.	(A3)
ES melding criterion	$\{\hat{\psi}_k \mid \min_{\hat{\psi}_k} J_k = \mathrm{tr}\,[\mathbf{P}_k^p(+)]$ using $[\mathrm{d}_0,\ldots,\mathrm{d}_k]\}$.	(A4)

The estimation is treated in real-time as a minimum error variance filtering problem (Table 3). Using the error subspace (ES) concepts, the optimum rank-p approximation of $\mathbf{P}$ is then the matrix $\mathbf{P}^p$ which minimizes the trace of the complementary covariance $\mathbf{P}^c$, difference between $\mathbf{P}$ and $\mathbf{P}^p$ (Eq. (A3)). This optimum is the dominant rank-p eigendecomposition of $\mathbf{P}$, $\mathbf{E}\,\Pi\,\mathbf{E}^T$. The ES is characterized by the dominant rank-p error eigenvectors and eigenvalues, $\mathbf{E}$ and Π. The filtering field estimate $\hat{\psi}_k$ (Eq. (A4)) hence minimizes the trace of the a posteriori error subspace covariance, based on past data and dynamics (Eqs. (A1), (A2), (A3) and (A4)).

The main quantities to be evolved are thus the field estimate, $\hat{\psi}$, and its principal error components and coefficients, $\mathbf{E}$ and Π. In this study, the scheme addressing Table 3 is recursive. It requires initial conditions for the fields, Ψ_0 (Section 2.3), and for the ES, $\mathbf{E}_0$ and Π_0 (Section 3.1). The main ESSE computations hence consist of four steps: the initialization of the ES (Section A.1), the assimilation or data-forecast melding (Section A.2), the adaptive learning of the dominant errors (Section A.3), and the state and ES forecasts to the next assimilation time (Section A.4). All quantities are dimensional except in the SVDs so that the ordering of singular values is unit independent. [3]

A.1. Error subspace initial conditions

The construction of the initial ES, summarized by Table 4, uses the PE model and data available on Sept. 15. The model errors assumed null (A1) and the initial data coverage being almost uniform in space (Fig. 4a), the dominant initial error covariance is assumed proportional to the dominant covariance of the PE variability with respect to Ψ_0. It is computed in two stages. The eigendecomposition of the covariance of the tracer variability is computed first, from data (Eqs. (A5), (A6), (A7), (A8), (A9), (A10) and (A11)). The dominant PE variability covariance is then estimated via adjustment PE integrations (Section 2.3), constructing the flow variability in accord with the dominant

[3] Quantities marked with asterisks are normalized. For each field, the norm is the volume and sample averaged variance. The SVDs are carried out on normalized matrices $\mathbf{M}^*$ such that $\mathbf{M} = \mathbf{N}\mathbf{M}^* = \mathbf{N}\mathbf{E}^*\Sigma\,\mathbf{V}^T$ and $\mathbf{E} = \mathbf{N}\mathbf{E}^*$, where the norm matrix $\mathbf{N} \in \mathbb{R}^{n\times n}$ is block diagonal. The notation $\mathrm{SVD}_p(\cdot)$ denotes the operator that carries out this normalization, selects the dominant rank p SVD and renormalizes the output, to yield $\mathbf{E}\,\Sigma\,\mathbf{V}^T$.

Table 4
Error subspace initialization (index $k = 0$ is omitted)

Tracer horizontal covariance eigendecomposition		
Normalized variability covariance matrix:	$\mathbf{C}^{r*}_{\rm trc} = \mathbf{E}^{r*}_{\rm trc}\, \Pi^{r*}_{\rm trc}\, \mathbf{E}^{r*T}_{\rm trc}.$	(A5)
Tracer vertical covariance eigendecomposition		
Historical (past synoptic) tracer residuals:	$\mathrm{d}^i_{\rm r} = \mathrm{d}^i - \mathrm{C}^i \hat{\psi}_{\rm trc},\ i = 1,\ldots,s.$	(A6)
Remove horizontal average, normalize:	$\mathrm{d}^{i*}_{\rm r} = N_{\rm r}^{-1}(\mathrm{d}^i_{\rm r} - \bar{\mathrm{d}}_{\rm r}).$	(A7)
SVD of the matrix of normalized tracer residuals:	$\mathrm{SVD}([\mathrm{d}^{1*}_{\rm r},\ldots,\mathrm{d}^{s*}_{\rm r}]) = \mathbf{E}^*_{\rm r}\, \Sigma^*_{\rm r}\, \mathbf{V}^{*T}_{\rm r}.$	(A8)
Tracer variability covariance matrix:	$\mathrm{C}^z_{\rm trc} = \mathbf{E}^z_{\rm trc}\, \Pi^z_{\rm trc}\, \mathbf{E}^{zT}_{\rm trc},\quad \text{where } \Pi^z_{\rm trc} = \Sigma^{*2}_{\rm r}/s.$	(A9)
Tracer 3D variability covariance eigendecomposition		
Kronecker product:	$\mathbf{P}_{\rm trc} = \mathrm{C}^z_{\rm trc} \otimes \mathrm{C}^{r*}_{\rm trc}.$	(A10)
Sort eigenvalues and truncate to subspace:	$\mathbf{P}^p_{\rm trc} = \mathbf{E}_{\rm trc}\, \Pi_{\rm trc}\, \mathbf{E}^T_{\rm trc}.$	(A11)
Primitive Equation Based Error Subspace		
Ensemble of perturbed initial tracer fields:	$\hat{\psi}^j_{\rm trc} = \hat{\psi}_{\rm trc} + \mathbf{E}_{\rm trc}\, \Pi^{\frac{1}{2}}_{\rm trc} \sqrt{q}\, \mathrm{e}^j,\quad j = 1,\ldots,q.$	(A12)
Differences of PE adjusted fields, normalize:	$\mathbf{M} = [\hat{\psi}^1_0 - \Psi_0,\ldots,\hat{\psi}^q_0 - \Psi_0];\quad M = NM^*.$	(A13)
SVD of normalized PE variability:	$\mathrm{SVD}(\mathbf{M}^*) = \mathrm{E}^* \Sigma^* \mathbf{V}^{*T}$	(A14)
Initial principal error covariance matrix estimate:	$\mathbf{P}^p = \gamma^2\, \mathrm{E}\, \Pi\, \mathrm{E}^T,\quad \text{with } \Pi = \Sigma^{*2}/q.$	(A15)

covariance of the tracer variability (Eqs. (A12), (A13), (A14) and (A15)). A factor scales the variability to an error variance.

In the first stage, the tracer variability covariance function is assumed separable in the horizontal and vertical. In the horizontal, the variability covariance matrices of $\boldsymbol{T}$ and $\boldsymbol{S}$, when normalized by their total variances, are presumed equal: $\mathbf{C}^{\mathbf{r}*}_{TT} = \mathbf{C}^{\mathbf{r}*}_{TS} = \mathbf{C}^{\mathbf{r}*}_{SS} = \mathbf{C}^{\mathbf{r}*}_{\rm trc}$, using a notation similar to that of Daley (1991), with the superscript $\mathbf{r}$ denoting the horizontal separation vector. In the present study, [4] the matrix $\mathbf{C}^{\mathbf{r}*}_{\rm trc} \in \mathbb{R}^{l_h \times l_h}$ is specified analytically, in accord with the horizontal scales seen in the data (Fig. 4a). Its eigende-composition (Eq. (A5)) is feasible and simply carried out. In the vertical, the decomposition of the dimensional tracer covariance matrix, $C^z_{\rm trc} \boldsymbol{\epsilon} \mathbb{R}^{2l_v \times 2l_v}$, is computed from EOFs of data residuals. The misfits between the initial profiles (Fig. 4a) and objectively analyzed tracers $\hat{\psi}_{\rm trc}$ are evaluated at data-points Eq. (A6). In Eq. (A6), the $\mathbf{d}^i$ contain the $i = 1,\ldots,s$ profiles linearly interpolated onto the $l_{\rm v}$ model levels. The $\mathbf{C}^i$ consist of horizontal bilinear interpolators. The horizontal averages $\bar{d}_{\rm r}$ of the residuals $\mathbf{d}^i_{\rm r}$ are then removed and the resulting zero-mean residuals normalized by their sample and

[4] The number of horizontal, vertical and total grid points are $l_{\rm h}$, $l_{\rm v}$ and $l \doteq l_{\rm h} l_{\rm v}$, respectively.

volume average, $d_r^i* = N_r^{-1}(d_r^i - \bar{d}_r)$ in Eq. (A7). The SVD of the matrix of normalized residuals (Eq. (A8)) is evaluated, which yields the tracer variability vertical EOFs and coefficients, $\mathbf{E}_{trc}^z = \mathbf{N}_r \mathbf{E}_r^*$ and $\Pi_{trc}^z = \Sigma_r^{*2}/s$, or dominant decomposition of $\mathbf{C}_{trc}^z$ (Eq. (A9)). Finally, including the scalar horizontal variances of T and S into $C_{trc}^z \epsilon \mathbb{R}^{2l_v \times 2l_v}$, the 3D covariance matrix $\mathbf{P}_{trc} \in \mathbb{R}^{2l \times 2l}$ is simply the Kronecker product $\mathbf{C}_{trc}^z \otimes \mathbf{C}_{trc}^{r*}$ (Eq. (A10)). The significant rank-p eigendecomposition of $\mathbf{P}_{trc}$, $\mathbf{E}_{trc}\,\Pi_{trc}\,\mathbf{E}_{trc}^T$ where $\mathbf{E}_{trc} \epsilon \mathbb{R}^{2l \times q}$ (Eq. (A11)), is then easily obtained from the eigendecompositions of $\mathbf{C}_{trc}^z$ and $\mathbf{C}_{trc}^{r*}$ (Graham, 1981).

In the second stage, an ensemble of q tracer initial conditions, $\hat{\psi}_{trc}^j$, of covariance matrix (Eq. (A11)) is first created (Eq. (A12)). The fields $\hat{\psi}_{trc}^j$ are obtained by adding to $\hat{\psi}_{trc}$ an adequately weighted eigenvector j, $\mathbf{E}_{trc}\,\Pi_{trc}^{1/2}\,\sqrt{q}\,\mathbf{e}^j$, where the $\mathbf{e}^j$'s are $j = 1,\ldots,q$ base vectors. The resulting states are then balanced by an ensemble of adjustment PE integrations: the perturbed tracer fields $\hat{\psi}_{trc}^j$ are fixed and the momentum equations in Eq. (A1) integrated forward until the mean kinetic energy stabilizes around a plateau, without rapid changes (parallel computing is then used). The differences between Ψ_0 and these PE adjusted fields $\hat{\psi}_0^j$ form the matrix $\mathbf{M}$ (Eq. (A13)). This matrix is normalized and the initial ES (Eq. (A15)) is estimated from the SVD of $\mathbf{M}^*$ (Eq. (A14)). During the parallel adjustment PE integrations, a similarity coefficient is evaluated (as in the ES forecast, Table 5 hereafter) to assess the added value of new integrations and thus decide at which j to stop. Finally, the factor γ^2 in Eq. (A15) scales the variability variance to an error variance.

A.2. Assimilation or data-forecast melding

The melding is chosen linear and based on a minimum error variance in the sample ES (Table 6). The present scheme being recursive, the sample ES forecast, described by $\mathbf{E}\_$ and $\Pi(-)$, is assumed available. It is obtained in Section A.4.

The update of the state (Eq. (A16)) uses the gain $\mathbf{K}^p$ (Eq. (A17)), optimal for the dominant error covariance forecast given by $\mathbf{E}\_$ and $\Pi(-)$. In Eq. (A18), $\Pi(+)$ is estimated by eigendecomposition of the right-hand-side: the columns of $\mathbf{H}$ are ordered orthonormal eigenvectors and $\Pi(+)$ is the ordered diagonal matrix of eigenvalues; $\mathbf{E}_+$ then follows from Eq. (A19).

A.3. Adaptive learning of the dominant errors

For several reasons, including the simple dynamical and measurement error models, the error subspace reduction and the linear melding, significant components of the ocean signal could be left over in the a posteriori residuals. Table 7 describes the discrete algorithm used here to learn (correct) the ES in accord with these possibly significant residuals. Continuous dynamical systems (e.g., Brockett, 1990) for such adaptive ES learning and ESSE assimilations can also be derived (Lermusiaux, 1997).

The a posteriori tracer residuals, $\mathbf{d} - \mathbf{C}\hat{\psi}(+)$, are first analyzed into gridded fields $\hat{n}(+)$, via a one-stage ESSE analysis (Eqs. (A20) and (A21)). The background for these

Table 5
Nonlinear dynamical state and ES ensemble forecast

State central forecast

$$\hat{\psi}_{k+1}(-) | \mathrm{d}\hat{\psi} = \mathbf{f}(\hat{\psi}, t)\mathrm{d}t, \text{ with } \hat{\psi}_k = \hat{\psi}_k(+). \tag{A24}$$

ES initial conditions

$$\hat{\psi}_k^j(+) = \hat{\psi}_k(+) + E_k(+)\Pi_k^{\frac{1}{2}}(+)u^j, \quad j = 1, \ldots, q, \tag{A25}$$

where $\mathbf{u} \in \mathbb{R}^{p \times 1}$ is random, of zero-mean and identity variance, constrained to yield $\hat{\psi}_k^j(+)$'s in accord with the measurement model (A1).

Ensemble forecast

$$\mathrm{d}\hat{\psi}^j = \mathbf{f}(\hat{\psi}^j, t)\mathrm{d}t, \text{ with } \hat{\psi}_k^j = \hat{\psi}_k^j(+), \quad j = 1, \ldots, q. \tag{A26}$$

ES forecast

$$M_{k+1}(-) = [\hat{\psi}_{k+1}^j(-) - \hat{\psi}_{k+1}(-)], \quad j = 1, \ldots, q,$$

decomposed into, $\Pi_{k+1}(-) \doteq \frac{1}{q}\Sigma_{k+1}^2(-)$ and $\mathbf{E}_{k+1}(-)$ of rank $p \leq q$, defined by,

$$\{\Sigma_{k+1}(-), \mathbf{E}_{k+1}(-) | \mathrm{SVD}_p(\mathbf{M}_{k+1}(-)) = \mathbf{E}_{k+1}(-)\Sigma_{k+1}(-)\mathbf{V}_{k+1}^T(-)\}, \tag{A27}$$

Convergence criterion

$$\rho = \frac{\sum_{i=1}^{le} \sigma_i\left(\Pi^{\frac{1}{2}} E^T \tilde{E} \tilde{\Pi}^{\frac{1}{2}}\right)}{\sum_{i=1}^{\tilde{p}} \sigma_i(\tilde{\Pi})} \geq \alpha, \tag{A28}$$

where α is a chosen convergence limit $(1 - \epsilon \leq \alpha \leq 1)$, $k = \min(\tilde{p}, p)$ and $\sigma_i(\cdot)$ selects the singular value number i.

fields, $\hat{n}(-)$, is null. The corresponding tracer error covariance decomposition, $\Pi_{\mathrm{trc}}(-)$ and $\mathbf{E}_{\mathrm{trc}}(-)$, is constructed following the first-stage (Eqs. (A5), (A6), (A7), (A8), (A9), (A10) and (A11)) of Section A.1. The assumptions are: (1) separability in the vertical/horizontal, (2) analytical horizontal correlation, in accord with the horizontal scales seen in the residuals, (3) vertical covariance matrix computed from the vertical EOFs of the residuals. The resulting fields $\hat{n}(+)$ are then used to update the a posteriori ES obtained in Eqs. (A18) and (A19). They form a new column of the error sample

Table 6
Minimum sample ES variance, linear update (subscript k omitted)

Dynamical state update:

$$\hat{\psi}(+) = \hat{\psi}(-) + \mathbf{K}^{p}(\mathbf{d} - \mathbf{C}\hat{\psi}(-)). \tag{A16}$$

Sample ES Optimal Gain:

$$\mathbf{K}^{p} = \mathbf{E}_{-}\, \Pi(-)C^{p^T}(\mathbf{C}^{p}\Pi(-)\mathbf{C}^{p^T} + \mathbf{R})^{-1}, \quad \text{where } \mathbf{C}^{p} \doteq \mathbf{C}\mathbf{E}_{-}. \tag{A17}$$

Sample ES Cov. Update:

$$\mathbf{H}\,\Pi(+)\mathbf{H}^T = \Pi(-) - \Pi(-)\mathbf{C}^{p^T}(\mathbf{C}^{p}\Pi(-)\mathbf{C}^{p^T} + \mathbf{R})^{-1}\mathbf{C}^{p}\Pi(-). \tag{A18}$$

$$\mathbf{E}_{+} = \mathbf{E}_{-}\,\mathbf{H}. \tag{A19}$$

matrix $[E_{+}\Sigma(+), \hat{n}(+)] \epsilon \mathbb{R}^{n\times(p+1)}$. At each assimilation time t_k, the size of the current ES is increased by one and the dominant error decomposition re-evaluated (Eqs. (A22) and (A23)).

In Eqs. (A22) and (A23), $\mathbf{E}^{\mathrm{a}}_{+}$ and $\Pi^{\mathrm{a}}(+)$ are the adapted error vectors and values, which have learned the significant tracer a posteriori residuals. In Section A.4, we refer to this adapted ES simply as the ''a posteriori ES'', without the superscript a.

A.4. State and ES forecasts

The quantities $\hat{\psi}_k(+)$, $\mathbf{E}_k(+)$ and $\Pi_k(+)$, obtained in Sections A.2 and A.3, are now forecast to t_{k+1}. The state forecast $\psi_{k+1}(-)$ is here set to the central forecast (Eq. (A24)), which is the first-order estimate of the statistical mean state (Jazwinski, 1970). The ES is evolved by integrating to t_{k+1} an ensemble of $j = 1, \ldots, q$ perturbed states,

Table 7
Adaptive learning of the error subspace (subscript k omitted)

$$\hat{n}(+) = \mathbf{K}_{\mathrm{trc}}(\mathbf{d} - \mathbf{C}\hat{\psi}(+)), \tag{A20}$$

$$\mathbf{K}_{\mathrm{trc}} = \mathbf{E}_{\mathrm{trc}}(-)\,\Pi_{\mathrm{trc}}(-)\mathbf{C}^{T}_{\mathrm{trc}}(\mathbf{C}_{\mathrm{trc}}\,\Pi_{\mathrm{trc}}(-)\mathbf{C}^{T}_{\mathrm{trc}} + \mathbf{R})^{-1}, \quad \text{where } \mathbf{C}_{\mathrm{trc}} \doteq \mathbf{C}\mathbf{E}_{\mathrm{trc}}(-). \tag{A21}$$

$$\mathbf{E}^{a}_{+}\,\Sigma^{a}(+)\mathbf{V}^{aT}_{+} = \mathrm{SVD}_{p+1}([\mathbf{E}_{+}\,\Sigma(+), \hat{\mathbf{n}}(+)]), \tag{A22}$$

$$\Pi^{a}(+) = \frac{1}{q+1}\Sigma^{a2}(+). \tag{A23}$$

$\hat{\psi}_k^j(+)$, that sample the a posteriori error vectors $\mathbf{E}_k(+)$ with variances $\Pi_k(+)$; the ensemble covariance matrix from $\hat{\psi}_k(+)$ then tends to $\mathbf{P}_k^p(+)$ for $q \to \infty$ (Eq. (A25)). The data residuals of all $\hat{\psi}_k^j(+)$'s are here also constrained to be in close accord with the measurement errors: the $\hat{\psi}_k^j(+)$ which have residuals of horizontal-averaged variance larger than twice the local data error variance are rejected (Eq. (A25)). While ensemble forecasts are computed in parallel (Eq. (A26)), the SVD of the current error forecast matrix, $M_{k+1}(-) = [\hat{\psi}_{k+1}^j(-) - \hat{\psi}_{k+1}(-)] \epsilon \mathbb{R}^{n \times q}$, is evaluated (Eq. (A27)). Integrations are stopped when the dominant SVD of these error samples stabilizes. This is here measured by the similarity coefficient ρ defined by Eq. (A28), where $(\mathbf{E}, \Pi)$ of rank p and $(\tilde{E}, \tilde{\Pi})$ of rank $\tilde{p} \geq p$ define ''previous'' and ''new'' estimates of the ES forecast, respectively. When ρ is close enough to one, the resulting $(\tilde{E}, \tilde{\Pi})$ determine the ES forecast for t_{k+1}, $(\Pi_{k+1}(-), \mathbf{E}_{k+1}(-))$, to be used as in Section A.2. The dimensions of the ensemble (q) and ES (p) hence vary with time, in accord with data and dynamics. In passing, the nonlinearities ensure that each new linearly perturbed state $\hat{\psi}_k^j(+)$ (Eq. (A25)) has the potential to add new value to the ES forecast.

References

Bennett, A.F., 1992. Inverse methods in physical oceanography. Cambridge Monographs on Mechanics and Applied Mathematics, Cambridge Univ. Press.

Böhm, E., Magazzu, G., Wald, L., Zoccolotti, M.-L., 1987. Coastal currents on the Sicilian shelf south of Messina. Oceanologica Acta 10 (2), 137–142.

Brockett, R.W., 1990. Dynamical systems that learn subspaces. In: Mathematical Systems Theory: The Influence of R.E. Kalman, Springer, pp. 410–420.

Burgers, G., P.J. van Leeuwen and G. Evensen, 1998. On the analysis scheme in the ensemble Kalman Filter. Mon. Weather Rev., accepted for publication, available from http://www.nrsc.no/geir.

Cane, M.A., Kamenkovich, V.M., Krupitsky, A., 1998. On the utility and disutility of JEBAR. J. Phys. Oceanogr. 28 (3), 519–526.

Cane, M.A., Kaplan, A., Miller, R.N., Tang, B., Hackert, E.C., Busalacchi, A.J., 1996. Mapping tropical Pacific sea level: data assimilation via a reduced state space Kalman filter. J. Geophys. Res. 101 (C10), 22599–22617.

Cohn, S.E., Todling, R., 1996. Approximate Kalman filters for stable and unstable dynamics. J. Meteor. Soc. Jpn. 74, 63–75.

Cox, M.D., 1984. A primitive equation, 3-dimensional model of the ocean. Technical Report. Geophysical Fluid Dynamical Laboratory/NOAA, Princeton.

Daley, R., 1991. Atmospheric Data Analysis. Cambridge Univ. Press.

Defant, A., 1961. Physical oceanography. Pergamon Press, New York.

Evensen, G., 1994. Inverse methods and data assimilation in nonlinear ocean models. Physica D 77, 108–129.

Flierl, G.R., Robinson, A.R., 1977. XBT measurements of thermal gradients in the MODE Eddy. J. Phys. Oceanogr. 7 (2), 300–302.

Garabedian, P.R., 1964. Partial Differential Equations. Wiley, New York, NY.

Gelb, A. (Ed.), 1974. Applied Optimal Estimation. MIT Press, Cambridge, MA.

Ghil, M., Malanotte-Rizzoli, P., 1991. Data assimilation in meteorology and oceanography. Advances in Geophysics, 33, Academic Press, 141–266.

Graham, A., 1981. Kronecker products and matrix calculus: with applications. Ellis Horwood, Halsted Press, a division of Wiley.

Jazwinski, A.H., 1970. Stochastic Processes and Filtering Theory, Academic Press.

Lermusiaux, P.F.J. 1997. Error Subspace Data Assimilation Methods for Ocean Field Estimation: Theory, Validation and Applications. PhD Thesis. May 1997. Harvard Univ. Cambridge, MA.

Lermusiaux, P.F.J., Robinson, A.R., 1998. Data assimilation via Error Subspace Statistical Estimation et al.Statistical Estimation, Part I: Theory and Schemes. Month. Weather Rev. in press.

Lermusiaux, P.F.J. 1998. Data assimilation via Error Subspace Statistical Estimation, Part II: Mid-Atlantic Bight Shelfbreak Front Simulations and ESSE validation. Month. Weather Rev., in press.

Lermusiaux, P.F.J., Anderson, D.G., Lozano, C.J., 1998. On the mapping of multivarite geophysical fields: error and variability subspace initial estimates. Q. J. R. Meteorol. Soc., sub-judice.

Lozano, C.J., Haley, P.J., Arango, H.G., Sloan Q., Robinson, A.R., 1994. Harvard coastal/deep water primitive equation model. Harvard Open Ocean Model Reports No. 52. Harvard Univ., Cambridge, MA.

Lozano, C.J., Robinson, A.R., Arango, H.G., Gangopadhyay, A., Sloan, N.Q., Haley P.J., Leslie, W.G., 1996. An interdisciplinary ocean prediction system: Assimilation strategies and structured data models. Modern approaches to data assimilation in oceano modelling. In: Malanotte-Rizzoli, P. (Ed.), Elsevier Oceanography Series, Elsevier, Amsterdam.

MacCready, P., Rhines, P., 1993. Slippery bottom boundary layers on a slope. J. Phys. Oceanogr. 23, 5–22.

Malanotte-Rizzoli, P. (Ed.), 1996. Modern Approaches to Data Assimilation in Oceano Modelling. Elsevier Oceanography Series, Elsevier, Amsterdam.

Miller, R.N., Carter, E.F., Blue, S.T., 1998. Data assimilation into nonlinear stochastic models. Available from http://tangaroa.oce.orst.edu/stochast.html.

Mellor, G.L., Wang, X.H., 1996. Pressure compensation and the bottom boundary layer. J. Phys. Oceanogr. 26 (10), 2214–2222.

Mertz, G., Wright, D.G., 1992. Interpretations of the JEBAR term. J. Phys. Oceanogr. 22, 301–305.

Moretti, M., Sansone, E., Spezie, G., De Maio, A., 1993. Results of investigations in the Sicily Channel (1986–1990). Deep-Sea Res. II 40 (6), 1181–1192.

Munk, W., 1981. Internal waves and small-scale processes, In: Warren, B.A., Wunsch, C. (Eds.), Evolution of Physical Oceanography. Scientific Surveys in Honor of Henry Stommel, 264–291.

Onken, R., Sellschopp, J., 1998. Seasonal variability of flow instabilities in the Strait of Sicily. J. Geophys. Res. 103 (C11), 24799–24820.

Orlanski, I., 1976. A simple boundary condition for unbounded hyperbolic flows. J. Comput. Phys. 41, 251–269.

Pouliquen, E. (Ed.), 1997. Rapid environmental assessment. SACLANTCEN Conference Proceedings Series CP-44, 290 pp.

Robinson, A.R., Golnaraghi, M., Leslie, W.G., Artegiani, A., Hecht, A., Lazzoni, E., Michelato, A., Sansone, E., Theocharis, A., 1991. Ünlüata, Ü., 1991. The eastern Mediterranean general circulation: features, structure and variability. Dynamics of Atmosphere and Oceans 15 (35), 215–240.

Robinson, A.R., Malanotte-Rizzoli P. (guest Eds.), 1993. Topical studies in oceanography. In: Milliman, J.D. (Ed.), Deep-Sea Research II, 40 (6) 1073–1329.

Robinson, A.R., 1996. Physical processes, field estimation and an approach to interdisciplinary ocean modeling. Earth Sci. Rev. 40, 3–54.

Robinson, A.R., Arango, H.G., Warn-Varnas, A., Leslie, W.G., Miller, A.J., Haley, P.J., Lozano, C.J., 1996. In: Malanotte-Rizzoli, P. (Ed.), Real-time Regional Forecasting in Modern Approaches to Data Assimilation in Ocean Modeling. Elsevier, Amsterdam.

Robinson, A.R., Lermusiaux, P.F.J., Sloan, N.Q., III, 1998a. Data Assimilation, in The Sea: The Global Coastal Ocean I. In: Brink, K.H., Robinson, A.R. (Eds.), Processes and Methods, Vol. 10, Wiley, New York.

Robinson, A.R., Sellschopp, J., Warn-Varnas, A., Leslie, W.G., Lozano, C.J., Haley, P.J., Jr., Anderson L.A., Lermusiaux, P.F.J., 1998b. The Atlantic Ionian Stream. J. Marine Systems, in press.

Robinson et al., 1998c. The Rapid Response 96, 97 and 98 exercises: The Strait of Sicily, Ionian Sea and Bay of Cadiz. Harvard Open Ocean Model Reports, Reports in Meteorology and Oceanography, Number 57.

Sellschopp J., Robinson, A.R., 1997. Describing and forecasting ocean conditions during operation rapid response. In: Pouliquen, E. (Ed.), Rapid Environmental Assessment. SACLANTCEN Conference Proceedings Series CP-44, 290 pp.

Shapiro, R., 1970. Smoothing, filtering, and boundary effects. Rev. Geophys. Space Phys. 8 (2), 359–387.

Sloan, N.Q., 1996. Dynamics of a Shelf/Slope Front: Process Studies and Data-Driven Simulations. PhD Thesis, May 1996, Harvard Univ. Cambridge, MA.

Sundqvist, H. (Ed.), 1993. Special Issue on Adjoint Applications in Dynamic Meteorology. Tellus, Series A: Dynamic Meteorology and Oceanography, 45A (5) 341–569.

Turner, J.S., 1981. Small-scale mixing processes. In: Warren, B.A., Wunsch, Carl (Eds.), Evolution of Physical Oceanography, Scientific Surveys in Honor of Henry Stommel, 236–262.

Warn-Varnas, A., Sellschopp, J., Haley, P.J., Jr., Leslie W.G., Lozano, C.J., 1998. Strait of Sicily Water Masses. Submitted Dynamics of Atmospheres and Oceans, Special Issue in honor of Prof. A.R. Robinson.

Wunsch, C., 1997. The Ocean Circulation Inverse Problem. Cambridge Univ. Press.